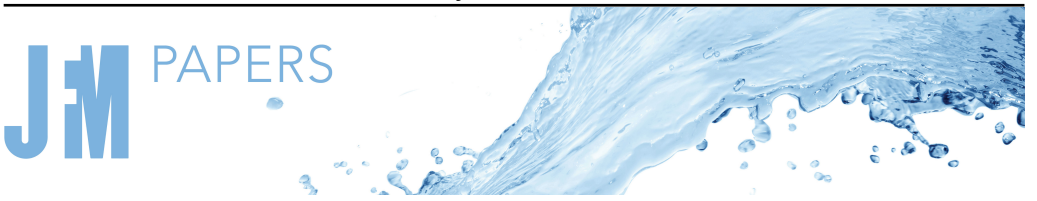
J. Fluid Mech. (2025), *vol.* 1025, A3, doi:10.1017/jfm.2025.10513



Compact Navier–Stokes trefoils in large domains with finite dissipation

Robert M. Kerr

Department of Mathematics, University of Warwick, Coventry CV4 7AL, UK

Corresponding author: Robert M. Kerr, robert.kerr@warwick.ac.uk

(Received 4 October 2024; revised 15 July 2025; accepted 15 July 2025)

For a perturbed trefoil vortex knot evolving under the Navier–Stokes equations, a sequence of ν-independent times t_m are identified that correspond to a set of scaled, volume-integrated vorticity moments $\nu^{1/4}\mathcal{O}_{Vm}$, with this hierarchy $t_\infty \leqslant \ldots \leqslant t_m \ldots t_1 = t_x \approx 40$ and $\mathcal{O}_{Vm} = (\int_{V_\ell} |\omega|^{2m}\, \mathrm{d}V)^{1/2m}$. For the volume-integrated enstrophy $Z(t)$, convergence of $\sqrt{\nu}Z(t) = \left(\nu^{1/4}\mathcal{O}_{V1}(t)\right)^2$ at $t_x = t_1$ marks the end of reconnection scaling. Physically, reconnection follows from the formation of a double vortex sheet, then a knot, which splits into spirals. Meanwhile Z accelerates, leading to approximate finite-time ν-independent convergence of the energy dissipation rate $\epsilon(t) = \nu Z(t)$ at $t_\epsilon \sim 2t_x$. This is sustained over a finite temporal span of at least $\Delta T_\epsilon \searrow 0.5t_\epsilon$, giving Reynolds number independent finite-time, temporally integrated dissipation, $\Delta E_\epsilon = \int_{\Delta T_\epsilon} \epsilon\, \mathrm{d}t$, and thus satisfies one definition for a dissipation anomaly, with enstrophy spectra that are consistent with transient $k^{1/3}$ Lundgren-like inertial scaling over some of the ΔT_ϵ time. A critical factor in achieving these temporal convergences is how the computational domain $V_\ell = (2\ell\pi)^3$ is increased as $\ell \sim \nu^{-1/4}$, for $\ell = 2$ to 6, then to $\ell = 12$, as ν decreases. Appendix A shows compatibility with established $(2\pi)^3$ mathematics where $\nu \equiv 0$ Euler solutions bound small ν Navier–Stokes solutions. Two spans of ν are considered. Over the first factor of 25 decrease in ν, most of the $\nu^{1/4}\mathcal{O}_{Vm}(t)$ converge to their respective t_m. For the next factor of 5 decrease (125 total) in ν, with increased ℓ to $\ell = 12$, there is initially only convergence of $\nu^{1/4}\Omega_{V\infty}(t)$ to t_∞, without convergence for $9 > m > 1$. Nonetheless, there is later $\sqrt{\nu}Z(t)$ convergence at $t_1 = t_x$ and $\epsilon(t) = \nu Z$ over $t \sim t_\epsilon \approx 2t_x$.

Key words: vortex dynamics, Navier-Stokes equations, turbulence simulation

© The Author(s), 2025. Published by Cambridge University Press. This is an Open Access article, distributed under the terms of the Creative Commons Attribution licence (https://creativecommons.org/licenses/by/4.0/), which permits unrestricted re-use, distribution and reproduction, provided the original article is properly cited.

https://doi.org/10.1017/jfm.2025.10513 Published online by Cambridge University Press

1. Introduction

Finite-energy dissipation is ubiquitous in turbulent, large-Reynolds-number, geophysical and engineering flows. Therefore, in these systems, observations show that their turbulent flows always develop Reynolds number, or viscosity ν, independent dissipation (Sreenivasan 1984; Vassilicos 2015). Forced simulations can generate finite-dissipation, but it is unclear what the pre-cursors to finite-dissipation might be if the flow is unforced. Can trefoil reconnection calculations (Kerr 2018*b*, 2023) fill that gap?

To answer that question, this paper introduces this pre-cursor for trefoil knot analysis: temporal convergence of $\nu^{1/4}$ scaled, volume-integrated vorticity moments, $\nu^{1/4}\mathcal{O}_{Vm}(t)$, with

$$\mathcal{O}_{Vm}(t) = \left(\int_{\mathcal{V}} |\omega|^{2m} \, \mathrm{d}V \right)^{1/2m} \quad \text{and} \quad \mathcal{O}_{V1} \leqslant \ldots \leqslant d_{m-1}\mathcal{O}_{V(m-1)}(t) \leqslant d_m \mathcal{O}_{Vm}(t) \tag{1.1}$$

for $m < \infty$, with the role of $m = \infty$ treated differently (1.9). The hierarchy of convergence times is $t_\infty \leqslant \ldots \leqslant t_m \ldots t_1 = t_x$ and precedes the post-reconnection $t > t_x$ accelerated growth of the volume-integrated enstrophy $Z(t) = \mathcal{O}_{V1}^2(t)$ (1.13) that leads to finite dissipation, with evidence from figure 6 for a numerical dissipation anomaly.

The definition of a numerical dissipation anomaly in this paper is the convergence of this time-integral of the energy dissipation rate $\epsilon(t) = \nu Z(t)$ as ν decreases (Kerr 2023), with

$$\Delta E_\epsilon = \int_0^{\Delta T_\epsilon} \epsilon \, \mathrm{d}t > 0 \,, \quad \text{over a finite time } \Delta T_\epsilon. \tag{1.2}$$

Note that $Z(t) = V_\ell \Omega_1^2(t) = \mathcal{O}_{V1}^2$ (1.13), where Ω_1 is the standard first Sobolev vorticity moment (1.8).

This definition of a dissipation anomaly is a bit more stringent than some earlier definitions that state that it is sufficient that $\epsilon(t)$ remains finite (Yao & Hussain 2022). However, if the time-integral in (1.2) is the condition, those previous reconnection simulations all fail to generate finite ΔE_ϵ, with § 3.1 being more specific.

In answering the finite ΔE_ϵ (1.2) question, and whether these calculations are becoming turbulent, these secondary issues are also addressed.

(i) The two critical elements within the initial vorticity profiles responsible for the relative success of trefoil knots are that they are: (*a*) compact and (*b*) algebraic.

(ii) These elements are why these calculations differ from the majority of existing vortex reconnnection calculations (Yao & Hussain 2022).

(iii) Being compact allows the domain size $(2\ell\pi)^3$ to be increased, which has been essential for achieving finite ΔE_ϵ as ν decreases. The empirical dependence of ℓ upon ν is determined (2.1), and the Appendix A describes new mathematics that shows that this type of dependence is compatible with existing mathematics.

(iv) Being compact also allows the temporal convergences of the new volume-integrated moments $\mathcal{O}_{Vm}(t)$ (1.1) to form, with the $(2\ell\pi)^3$ domains growing as ν decreases.

(v) The strong acceleration of enstrophy $Z(t)$ that forms finite ΔE_ϵ (1.2) develops only after the last of those vorticity moment temporal convergences and without the formation of a statistically steady turbulent state or a traditional energy cascade. Which raises the following questions.

(vi) Is there evidence for a less-traditional energy cascade? For forced Navier–Stokes, the evidence for traditional cascades can come from observing statistically steady

https://doi.org/10.1017/jfm.2025.10513 Published online by Cambridge University Press

Kolmogorov $E_V(k) \sim k^{-5/3}$ spectra. An alternative is to follow the development of transient $k^{-5/3}$ spectra, or an equivalent, as finite ΔE_ϵ forms.

(vii) What type of model could explain that cascade's behaviour? For statistically steady turbulence, there are supporting models that assume that singularities control the cascades to the dissipation scales (Dubrulle 2019). Despite the accelerated, post-reconnection growth of the enstrophy, this trefoil never shows any signs of singular behaviour (Kerr 2018*b*). With this complementary question: Does achieving finite energy dissipation require statistically steady Kolmogorov scaling?

(viii) An incomplete example of an alternate time-evolving model is the spiral vortex model of Lundgren (1982). This is based upon the transient evolution of a perturbation about an axisymmetric, 2.5-dimensional compressed/stretched vortex. The primary result was that as the perturbations are pulled into sheets and compressed, they become spirals and the time-averaged spectra obey $E_{axi}(k) \sim k^{-5/3}$. One reason for why the model is incomplete is because it lacks a source for the imposed vortex stretching, with these and earlier calculations showing where that might originate. The model is relevant to these calculations due to these observations.

(ix) As the dissipation rates increase in figure 6, rolled-up vortex sheets in § 4 become the dominant structures, with § 3.2 showing that transient $Z_V(k) \sim k^{1/3}$ enstrophy spectra (3.1) form.

(x) Based on this, the scaling of the transient enstrophy spectra is called Lundgren-like, a designation that clarifies that the underlying dynamics during this stage does not have to be statistically steady, as discussed further in § 5.3.

What are the critical elements for these calculations? These are provided by two sets of unforced trefoil knot calculations (Kerr 2018*b*, 2023). Both used algebraic initial vorticity profiles and had modest ΔE_ϵ over modest (factor of 4–8) ratios of ν, but without corroborating analysis for turbulent scaling such as wavenumber spectra.

Kerr (2018*b*) was the first to report that to achieve greater enstrophy growth and numerical convergent dissipation rates, the domain size $\mathcal{L}$ had to be increased as the viscosity ν decreases (2.1), thus breaking the constraint imposed by using only $(2\pi)^3$ domains. This is now justified mathematically in the Appendix A.

Kerr (2023) then showed why, due to their improved stability properties, algebraic vorticity profiles rather than the traditional Gaussian vorticity profiles (Yao & Hussain 2022) should be used.

By combining those two elements over a range of small ν, moderately high-Reynolds-number Navier–Stokes simulations in large domains can, without forcing or parametrisations, get approximate temporal convergence of the dissipation rates $\epsilon(t) = \nu Z(t)$ at $t_\epsilon \approx 2t_x$ and consistent finite-time ΔE_ϵ, (1.2) at $t \sim 1.5t_\epsilon$, as well as address the additional secondary questions listed previously.

For comparing results from several computational domains, trefoil vortex knots with algebraic vorticity profiles are an ideal initial condition because they are compact, do not have inherent boundary instabilities and are interesting because the usual assumptions of isotropy are broken by the helical initial condition. Compact means that the trefoils can be isolated from the boundaries as both the energy and enstrophy profiles decay rapidly as $r \to \infty$, and can be redone in multiple domains.

The particular $p = 1$ algebraic profile (1.24) being used was introduced for several anti-parallel Navier–Stokes and Euler calculation in 2013 (Donzis *et al.* 2013; Kerr 2013*a*,*b*), used for several 2018 vortex knot calculations (Kerr 2018*a*,*b*,*c*) and for the primary calculations for three-fold symmetric trefoils (Kerr 2023). Figure 1, discussed further in

https://doi.org/10.1017/jfm.2025.10513 Published online by Cambridge University Press

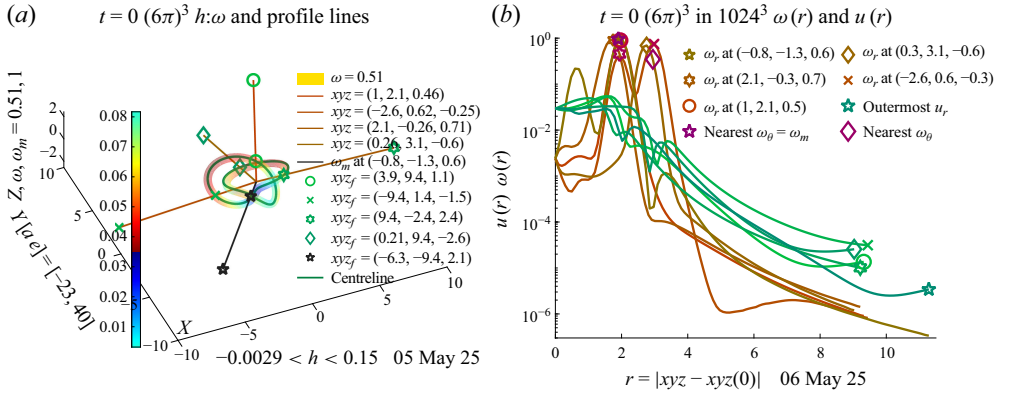


Figure 1. Perturbed trefoil initial condition. (*a*) $\omega = 0.51$ isosurface with $\omega_m = 1$ at $\star = (-0.8,\ -1.3,\ 0.6)$, centreline vortex line seeded at ω_m and several $\boldsymbol{s}_j(r)$ paths from the weighted centre of the trefoil, with each passing through the centreline vortex and on to the periodic boundaries. The legend gives their $\boldsymbol{s}_j(r)$ positions through the centreline vortex and their final $xyz_f = (x,\ y,\ z)_f$ positions on either the x or y periodic boundaries with $x = \pm 3\pi = \pm 9.4$ and $y = \pm 3\pi = \pm 9.4$. (*b*) Profiles of $|\boldsymbol{\omega}|_j(r)$ and $|\boldsymbol{u}|_j(r)$ taken along the $|\boldsymbol{s}|_j(r)$. For all paths, $\omega_j(r) \to 0$ exponentially as r grows. The $|\boldsymbol{u}|_j(r) \to 0$ exponentially for two decades, then flatten as the periodic boundaries are reached, where $\mathrm{d}|\boldsymbol{u}|_j/\mathrm{d}|\boldsymbol{s}|_j| \to 0$ is expected. Confirming that this initial condition is a reasonable approximation to being compact. The path through ω_m points into a corner, so is longer.

§ 1.4, demonstrates that this initial condition is compact, even though when this profile is applied to an isolated, straight vortex, the resulting fields are not compact.

Details of the stability properties of the algebraic profile on the trefoil using the original formulation of Howard & Gupta (1961) have been given previously (Kerr 2023). Essentially, what that formulation tells us is that a profile can be unstable if the Rayleigh inflection point criterion is violated. That instability does not develop when algebraic profiles are used (Kerr 2023), but can be formed for Gaussian/Lamb–Oseen profiles. However, 'can be' does not necessarily mean 'must be', and what determines that difference mathematically is whether the initial pertubations break through ill-defined critical layers (Gallay & Smets 2020).

Kerr (2023) showed that when mapping a strongly curved vortex trajectory onto a Cartesian mesh, the resulting field is not perfectly solenoidal and that after the necessary solenoidal correction is imposed, a large seed is created, one large enough to break through the critical layer, allowing the Gaussian profile instability to grow. This observation probably applies to most of the calculations discussed in a recent review (Yao & Hussain 2022). However, this seed does not form if the initial vortices in a three-dimensional fluid are straight as observed by Ostillo-Monico *et al.* (2021) and Zuccoli, Brambley & Barkley (2024). So there are still many situations when the use of a Gaussian profile is legitimate.

Is there an early time diagnostic, supported by mathematics, that shows whether increasing the domain is a viable approach? Fortunately, by using the volume-integrated enstrophy Z (1.13) as the diagnostic, instead of the volume-averaged enstrophy $Z_\Omega = \Omega_1^2$ (1.8), temporal convergence can be achieved using $\sqrt{\nu} Z(t)$ at intermediate fixed times $t = t_x$. With § 1.3 and Appendix A, we show that this empirical large-domain observation is compatible with, through rescaling, a previously strictly $(2\pi)^3$ analytic result (Constantin 1986).

Where have observations identified convergent energy dissipation? Historically, one means is to use controlled experiments of turbulent flows to determine a dissipation coefficient C_ϵ, obtained by comparing the measured dissipation rate ϵ with the large scale

https://doi.org/10.1017/jfm.2025.10513 Published online by Cambridge University Press

dimensional estimate as follows:

$$\epsilon = C_\epsilon \mathcal{U}^3/\mathcal{L} \sim C_\epsilon r_f^2/t_{NL}^3\,, \tag{1.3}$$

where $\mathcal{U}$ and $\mathcal{L}$ are the large-scale velocity and length (Vassilicos 2015). For the trefoil, one can use its diameter $\mathcal{L}=2r_f$ (1.23) and for a 'turbulent' velocity $\mathcal{U}$, one can choose $\mathcal{U}=\|u\|_\infty(t_\epsilon)$, the maximum velocity at t_ϵ, the time with the largest dissipation rate ϵ (1.12) from figure 6. This is also when spectra show brief signs of Lundgren scaling in § 3.2. Early grid turbulence and jet data showed that C_ϵ is independent of the Reynolds number (Sreenivasan 1984), a conclusion that could even be applied to non-equilibrium turbulence (Vassilicos 2015). However, recent results (Schmitt *et al.* 2024) suggest that the large-scale coefficient C_ϵ depends on the properties of the small scale intermittency. Those are the experimental results that are used for the comparisons in the inset of figure 6.

The paper is organised as follows. First, the equations are introduced, followed by a discussion of why simulations in large domains were required, including a summary of the new mathematics qualitatively supporting the previous empirical conclusions. This is followed by the extended numerical results for both $1/(\sqrt{\nu}Z(t))^{1/2}$ and $\epsilon(t)=\nu Z$ scaling, including evidence for a dissipation anomaly and additional examples of $t \lesssim t_x$, $\nu^{1/4}\mathcal{O}_{Vm}(t)$ convergence. Resolution requirements are mentioned in § 1.4 and discussed further in § 2.2. Section 3.2 provides the evidence for turbulent-like spectra. Section 4 presents three-dimensional vortices for $t=24$, 30, 42 and 48, mainly using helicity-mapped isosurfaces. At $t=48$, the vortices are coiled in a manner consistent with accelerating dissipation rates. Appendix A extends $(2\ell\pi)^3$, $\ell=1$ Sobolev H^s analysis to larger $\ell>1$, $(2\ell\pi)^3$ domains, showing that as ℓ grows, there is relaxation of the analytic/Sobolev critical viscosities ν_s that enforce bounds upon the evolution of still smaller viscosities. These ν_s decrease as ℓ increases, which in turn allows convergence of the dissipation rates $\epsilon=\nu Z$ as ν decreases.

1.1. *Governing equations*

This paper primarily uses the incompressible $\nu \sim Re^{-1} \neq 0$ viscous Navier–Stokes velocity equations

$$\frac{\partial \boldsymbol{v}}{\partial t} + (\boldsymbol{v}\cdot\boldsymbol{\nabla})\boldsymbol{v} = -\boldsymbol{\nabla} p + \underbrace{\nu\boldsymbol{\Delta v}}_{\text{viscous drag}}\,, \quad \boldsymbol{\nabla}\cdot\boldsymbol{v}=0\,, \tag{1.4}$$

and for additional analysis, the inviscid $\nu \equiv 0$ Euler equation

$$\frac{\partial \boldsymbol{u}}{\partial t} + (\boldsymbol{u}\cdot\boldsymbol{\nabla})\boldsymbol{u} = -\boldsymbol{\nabla} p. \tag{1.5}$$

This includes the equation for their difference $\boldsymbol{w}=\boldsymbol{v}-\boldsymbol{u}$, which by replacing $\boldsymbol{v}$ by $\boldsymbol{w}+\boldsymbol{u}$ throughout becomes

$$\boldsymbol{w}_t + \nu\Delta\boldsymbol{w} = -\nu\Delta\boldsymbol{u} - \underbrace{(\boldsymbol{w}\cdot\boldsymbol{\nabla})\boldsymbol{w}}_{B_{NL}(w,w)} - \underbrace{(\boldsymbol{u}\cdot\boldsymbol{\nabla})\boldsymbol{w}}_{B_{NL}(u,w)} - \underbrace{(\boldsymbol{w}\cdot\boldsymbol{\nabla})\boldsymbol{u}}_{B_{NL}(w,u)} - \boldsymbol{\nabla} p_w - \boldsymbol{\nabla} p_u. \tag{1.6}$$

The Constantin & Foias (1988) notation $B_{NL}(u,v)=(\boldsymbol{u}\cdot\boldsymbol{\nabla})\boldsymbol{v}$ has been added to emphasise the similarities between how the three nonlinear terms are treated in Appendix A.3.

The equation for the vorticity $\boldsymbol{\omega}=\boldsymbol{\nabla}\times\boldsymbol{v}$ is

$$\frac{\partial \boldsymbol{\omega}}{\partial t} + (\boldsymbol{v}\cdot\boldsymbol{\nabla})\boldsymbol{\omega} = (\boldsymbol{\omega}\cdot\boldsymbol{\nabla})\boldsymbol{v} + \nu\Delta\boldsymbol{\omega}, \qquad \boldsymbol{\nabla}\cdot\boldsymbol{\omega}=0. \tag{1.7}$$

https://doi.org/10.1017/jfm.2025.10513 Published online by Cambridge University Press

and in fixed domains V_ℓ, the usual $\Omega_m(t)$ vorticity moments are

$$\Omega_m(t) = \left(V_\ell^{-1} \int_{\mathcal{V}_\ell} |\omega|^{2m} \, \mathrm{d}V \right)^{1/2m} \quad \text{and obey this hierarchy} \tag{1.8}$$
$$\Omega_1(t) \leqslant c_2\Omega_2(t) \leqslant \ldots \leqslant c_m\Omega_m(t) \leqslant \ldots \leqslant c_\infty\Omega_\infty(t).$$

This ordering represents a type of Hölder inequality (Hölder inequality: for f and g, $\langle |fg| \rangle_\ell \leqslant \langle |f|^p \rangle_\ell^{1/p} \langle |g|^q \rangle_\ell^{1/q}$ for $1/p + 1/q = 1$. Now choose $f \equiv 1$ and $g = \omega^{2m-2}$, $q = m/(m-1)$, $p = m$. From which the c_m (1.8) and d_m (1.9) coefficients can be determined. See also Theorem 1.2 of Robinson, Rodrigo & Sadowski 2016) and whilst the c_m can be V_ℓ-dependent constants, for this definition of Ω_m, all the c_m are independent of V_ℓ, with each $c_m \equiv 1$. These moments, scaled by characteristic frequencies, have been used in several recent papers (Donzis *et al.* 2013; Kerr 2013*a*).

However, because multiple domains are used in this paper, the relevant moment hierarchy in this paper is for the $\mathcal{O}_{Vm}(t)$ (1.1) that uses volume integration. The inequality coefficients d_m between any adjacent moments with $\mathcal{O}_{V(m-1)}(t) \leqslant d_m\mathcal{O}_{Vm}$ are

$$d_m = V_\ell^{1/\left(m(2m-2)\right)} \quad \text{with } V_\ell^{1/2m}\|\omega\|_\infty \text{ bounding each } \mathcal{O}_{Vm}(t) \tag{1.9}$$

and the volume-integrated enstrophy can be written as $Z(t) = V_\ell\Omega_1^2(t) = \mathcal{O}_{V1}^2$. The only place that this definition of the enstrophy is not used is for estimating an effective Kolmogorov-dissipation wavenumber for figure 9(*d*).

For a compact vortex knot, the circulations Γ_i about its vortex structures are

$$\Gamma_i = \oint_{\mathcal{C}_i} \boldsymbol{v}_i \cdot \boldsymbol{r}_i \quad \text{where } \boldsymbol{r}_i \text{ is a closed loop about } \mathcal{C}_i. \tag{1.10}$$

Dimensionally, for a vortex knot of size r_f with velocity scale of U, the circulation goes as $\Gamma \sim U r_f$. In vortex dynamics, the circulation Reynolds number $R_\Gamma = \Gamma/\nu$ is widely used and for a vortex knot of size r_f, the nonlinear and viscous time scales are respectively

$$t_{NL} = r_f^2/\Gamma \quad \text{and} \quad t_\nu = r_f^2/\nu. \tag{1.11}$$

Three local densities are used. The energy density $e = (1/2)u^2$, the enstrophy density $\zeta = \omega^2$ and the helicity-density $h = \boldsymbol{u} \cdot \boldsymbol{\omega}$. Their budget equations, with their global integrals, are

$$\frac{\partial e}{\partial t} + (\boldsymbol{u} \cdot \boldsymbol{\nabla})e = -\underbrace{\boldsymbol{\nabla} \cdot (\boldsymbol{u}p)}_{\Pi = e-\text{flux}} + \nu\triangle e - \underbrace{\nu(\boldsymbol{\nabla}\boldsymbol{u})^2}_{\epsilon = \text{dissipation} = \nu Z}, \quad E_e = \frac{1}{2}\int_{\mathcal{V}_\ell} \boldsymbol{u}^2 \, \mathrm{d}V; \tag{1.12}$$

$$\frac{\partial \zeta}{\partial t} + (\boldsymbol{u} \cdot \boldsymbol{\nabla})|\boldsymbol{\omega}|^2 = \underbrace{2\boldsymbol{\omega}\boldsymbol{S}\boldsymbol{\omega}}_{\zeta_p = \text{production}} + \nu\triangle|\boldsymbol{\omega}|^2 - \underbrace{2\nu(\boldsymbol{\nabla}\boldsymbol{\omega})^2}_{\epsilon_\omega = Z-\text{dissipation}}, \quad Z = \int_{\mathcal{V}_\ell} \boldsymbol{\omega}^2 \, \mathrm{d}V; \tag{1.13}$$

$$\frac{\partial h}{\partial t} + (\boldsymbol{u} \cdot \boldsymbol{\nabla})h = \underbrace{-\boldsymbol{\omega} \cdot \boldsymbol{\nabla}\Pi}_{h_f = \omega-\text{transport}} + \underbrace{\nu\triangle h}_{\nu-\text{transport}} - \underbrace{2\nu\mathrm{tr}(\boldsymbol{\nabla}\boldsymbol{\omega} \cdot \boldsymbol{\nabla}\boldsymbol{u}^T)}_{\epsilon_h = \mathcal{H}-\text{dissipation}}, \quad \mathcal{H} = \int_{\mathcal{V}_\ell} \boldsymbol{u} \cdot \boldsymbol{\omega} \mathrm{d}V. \tag{1.14}$$

Note that $\Pi = p - (1/2)\boldsymbol{u}^2 \neq p_h$ and is not the pressure head $p_h = p + (1/2)\boldsymbol{u}^2$.

In this paper, the primary norms are related to the energy and enstrophy equations. In addition to the dissipation rate $\epsilon = \nu Z$ (underscore in (1.12)), the following two

https://doi.org/10.1017/jfm.2025.10513 Published online by Cambridge University Press

viscosity-based rescalings of the enstrophy Z (1.1) will be used:

$$\sqrt{\nu}Z(t) \quad \text{and} \quad B_\nu(t) = 1/(\sqrt{\nu}Z(t))^{1/2} = (\nu^{1/4}\mathcal{O}_{V1})^{-1}\,, \tag{1.15}$$

where $\mathcal{O}_{V1}$ is the first volume-integrated vorticity moment (1.1). The helicity budget is included because the helicity-density h is mapped onto the vorticity isosurfaces for potential comparisons with the isosurfaces of the three-fold symmetric trefoils (Kerr 2023), where its budget equation is discussed in detail.

Under $\nu \equiv 0$ Euler, both E_e (1.12) and $\mathcal{H}$ (1.14), the global helicity, are conserved, with the pressure gradients affecting only their local Lagrangian densities e and h. In contrast, the global enstrophy Z (1.13) is not an invariant, but grows in figure 2 due to vortex stretching, as discussed in § 2.1. Here, E_e and Z can be recast in terms to the first two Sobolev norms, H^0 and H^1, as defined in (1.22). Due to vortex stretching, initially all H^s, $s > 1$, tend to grow.

1.2. *Norms and inner products*

The mathematical analysis in the Appendix A uses Sobolev inner products and norms. These are formed from the Fourier-transformed components $\hat{\boldsymbol{v}}(\boldsymbol{k})$ of the velocity field $\boldsymbol{v}(\boldsymbol{x})$ in a variably sized periodic domain parametrised by ℓ with volume

$$V_\ell = (2\ell\pi)^3 \quad \text{with the wavenumbers } \boldsymbol{k} = \ell^{-1}\boldsymbol{n}\,, \tag{1.16}$$

which are written using three-dimensional integer vectors $\boldsymbol{n}$. These give this definition and equation for $\hat{\boldsymbol{v}}_{\boldsymbol{k}}$,

$$\boldsymbol{v}(\boldsymbol{x}) = \sum_{\boldsymbol{k}} \hat{\boldsymbol{v}}_{\boldsymbol{k}} e^{i\boldsymbol{k}\cdot\boldsymbol{x}}; \quad \frac{\mathrm{d}}{\mathrm{d}t}\hat{\boldsymbol{v}}_{\boldsymbol{k}}(t) = -\nu|k|^2\hat{\boldsymbol{v}}_{\boldsymbol{k}}(t) - i\,\boldsymbol{P}(\boldsymbol{k}) \sum_{\boldsymbol{k}'+\boldsymbol{k}''=\boldsymbol{k}} \hat{\boldsymbol{v}}_{\boldsymbol{k}'}(t)\cdot\boldsymbol{k}''\hat{\boldsymbol{v}}_{\boldsymbol{k}''}(t). \tag{1.17}$$

The projection factor operator $\boldsymbol{P} = \boldsymbol{I} - \boldsymbol{k}\otimes\boldsymbol{k}/k^2$ incorporates the pressure in Fourier space.

The inner products come from multiplying the active equation by a test function, usually a velocity, in either real or Fourier space. After integrating that over all space, the inner products are

$$\langle u, v\rangle_\ell = \int_{\mathcal{V}_\ell} |\boldsymbol{u}\cdot\boldsymbol{v}|\,\mathrm{d}^3x, \quad \text{which are norms when } \boldsymbol{v} = \boldsymbol{u} \text{ with } \|u_\ell\|^2 := \langle u, u\rangle_\ell. \tag{1.18}$$

This paper uses s-order $\dot{H}^s = \dot{H}^s_{2\ell\pi}$ inner products that in a $\ell = 1$, $V_1 = (2\pi)^3$ domain are determined by the power of $|k|^{2s}$ as follows:

$$\langle u, v\rangle_{1\dot{s}} = \int_{\mathcal{V}_1} |\boldsymbol{\nabla}^s\boldsymbol{u}(x)\cdot\boldsymbol{\nabla}^s\boldsymbol{v}(x)|\,\mathrm{d}^3x = (2\pi)^3\sum_{\boldsymbol{k}} |k|^{2s}|\hat{\boldsymbol{u}}_{\boldsymbol{k}}(t)\cdot\bar{\hat{\boldsymbol{v}}}_{\boldsymbol{k}}(t)|\,, \tag{1.19}$$

with this further definition for $\ell \neq 1$: $\|u_\ell\|^2_{\dot{s}} := \|u_\ell\|^2_{\dot{H}^s}$.

The Navier–Stokes Fourier equation of the inner product of the $s = 0$, $\ell = 1$ norm $\|u\|_0^2$ is particularly simple. Due to incompressibility, and by using integration by parts to remove the pressure, this inner product equation reduces to

$$\frac{\mathrm{d}}{\mathrm{d}t}\frac{1}{2}\sum_{\boldsymbol{k}}|\hat{\boldsymbol{u}}_{\boldsymbol{k}}(t)|^2 = -\nu\sum_{\boldsymbol{k}}|\boldsymbol{k}|^2|\hat{\boldsymbol{u}}_{\boldsymbol{k}}(t)|^2 \quad \Rightarrow \quad \frac{\mathrm{d}}{\mathrm{d}t}\frac{1}{2}\|u\|_0^2 = -\nu\|\boldsymbol{\nabla}u\|_0^2 = -\nu\|u\|_1^2 \tag{1.20}$$

This set of equations demonstrates the simplification provided by taking inner products, with the discussion in Appendices A.1–A.6 using the form on the right. Doering (2009)

https://doi.org/10.1017/jfm.2025.10513 Published online by Cambridge University Press

provides a fluids-oriented review of these relations for simple geometries whilst Robinson *et al.* (2016) provide more complete details of the mathematics.

The ℓ-domain second-order s, squared H^s_ℓ Sobolev norms of u, v and $w = v - u$ (1.6) can be defined using the $L^{(2)}_\ell$ and the $\dot{H}^s_\ell$ norms as

$$\left(H^s_\ell\right)^2 = \|u_\ell\|^2_s = \|u\|^2_{H^s_\ell} = \|u\|^2_{L^{(2)}_\ell} + \|u\|^2_{\dot{H}^s_\ell} \tag{1.21}$$

where $\|u\|^2_{L^{(2)}_\ell} = (2\ell\pi)^{-3} \int |u|^2 \, \mathrm{d}x$ is the $\|u_\ell\|^2_0$ inner product in a $(2\ell\pi)^3$ domain and the squared $\dot{H}^s_\ell$ norms are

$$\left(\dot{H}^s_\ell\right)^2 = \|u_\ell\|^2_{\dot{s}} = \|u_\ell\|^2_{\dot{H}^s_\ell} = (2\pi)^3 \ell^{3-2s} \sum_{k \in \dot{\mathbb{Z}}^3} |k|^{2s} |\hat{\boldsymbol{u}}(k)|^2 = \ell^{3-2s} \|\nabla^s u\|^2. \tag{1.22}$$

In Appendix A, for the higher-order s norms, inequalities typically replace equalities like those in (1.20) and from this point onwards, all inner products are assumed to be $L^{(2)}_\ell$, and the upper $\dot{s}$ superscript will refer to the $\dot{H}^s$ inner products and norms.

The physical dimensions of the velocity norms, including the volume, are $\mathrm{Dim}[\|u\|_{\dot{s}}] = [\mathcal{L}^{5/2-s}/T]$ for a chosen length scale $\mathcal{L}$ and time scale T.

1.3. *Mathematics for large $(2\ell\pi)^3$ domains*

A potential drawback of using periodic domains of any size is that there is a set of $(2\pi)^3$ mathematical bounds from applied analysis of the Navier–Stokes equations (Constantin 1986) that are largely unknown to the general fluid dynamics community that, with further theorems, restrict the growth of the enstrophy as ν decreases.

What was shown was that the growth of all higher-order Sobolev norms under $\nu \neq 0$ Navier–Stokes are controlled by integrals of equivalent $\nu \equiv 0$ Euler norms as the viscosities become very small. More precisely, from $\nu \equiv 0$ Euler solutions $u(t)$, analytic critical viscosities ν_s can be determined from time-integrals of the higher-order $s \geqslant 5/2$, Sobolev norms $H^s(u)$. These in turn control the growth of the equivalent $H^s(v)$ of $\nu_s \geqslant \nu \neq 0$ Navier–Stokes solutions $v(t)$.

From there, additional embedding theorems (Robinson *et al.* 2016) can then be used to show that the dissipation rate $\epsilon = \nu Z \to 0$ (1.12), unless there are singularities of either the Navier–Stokes or Euler equations. Simplified, the steps are to take the bounds upon the $H^s(v)$, apply them to embedding theorems that can bound $\|\omega\|_\infty$, from which the vorticity moment hierarchies will bound $\mathcal{O}_{V1}$ (1.1), Ω_1 (1.8) and Z (1.13), from which $\epsilon = \nu Z \to 0$ as $\nu \to 0$ follows. This result is not relevant when, $\nu > \nu_s$, that is, if the viscosity is above the critical values ν_s.

Those results would include the evolution of all initial value (Cauchy) calculations done in strictly $(2\pi)^3$ domains and explain why very small ν, $(2\pi)^3$ calculations consistently fail to generate evidence for a dissipation anomaly with finite ΔE_ϵ (1.2), which is applicable to many calculations in addition to those cited by Yao & Hussain (2022).

Appendix A here modifies those $(2\pi)^3$ results for larger $(2\ell\pi)^3$ domains and shows that the suppression can be mitigated by doing small ν calculations in ever larger periodic domains because the viscosity-based ν_s bounds upon the growth of vorticity moments decrease as the domain parameter ℓ increases to accommodate decreasing ν.

The basic elements of the proof will follow a recent alternative to the classic result of Constantin (1986) given in Chapter 9 of Robinson *et al.* (2016). The revisions of the original 1986 proof fill in many gaps with essential details that did not appear until provided by Constantin & Foias (1988). One of these is a robustness proof that is then

https://doi.org/10.1017/jfm.2025.10513 Published online by Cambridge University Press

$\tilde{\nu}(\nu \times 10^5)$	50	25	12.5	6.25	6.25	3.125	3.125	2.2	1.6	0.78	0.4
$Re_\Gamma = \Gamma/\nu$	1010	2020	4040	8080	8080	16 160	16 160	22 954	32 372	64 744	126 250
Domain	$(4\pi)^3$	$(4\pi)^3$	$(4\pi)^3$	$(4\pi)^3$	$(6\pi)^3$	$(4\pi)^3$	$(6\pi)^3$	$(6\pi)^3$	$(6\pi)^3$	$(9\pi)^3$	$(12\pi)^3$
Adequate	Good	Good	Good	Good	Good	Not	Good	Good	Good	Good	Good
Mesh	1024^3	1024^3	1024^3	1024^3	2048^3	1024^3	2048^3	2048^3	2048^3	2048^3	2048^3
Resolved	Yes	Yes	Yes	Yes	Yes	Yes	Yes	Yes	No	No	No
Symbols	X	$*$	□	◯	⊗	$+$	△	$\star$	—	—	—
Colours	Black	Blue	Red	Mag	Purple	Brown	Green	Maroon	Lime	Orange	Cobalt

Table 1. Perturbed trefoil cases parameters. Rows, $\tilde{\nu} = \nu \times 10^5$. Domain, size of periodic domain. Adequate, asking whether the computational domain is large enough based upon ℓ_c (2.1). Mesh, computational meshes. Resolved, asking whether the given mesh resolves the flow in DNS mode. Symbols, for each case. Colours, for each case. mag = magenta.

inserted where needed into the final proof. Appendix A here then rescales the $(2\pi)^3$ results by assuming that the time scales and Reynolds numbers are invariant as the $\mathcal{L} = 2\ell\pi$, $(\mathcal{L})^3$ domains are increased. Finally, rather than just saying that certain very small critical viscosities exist, assumptions are made that suggest their magnitudes.

1.4. *Trefoil initial condition and numerics*

The trefoil vortex knot in this paper at $t = 0$ is defined as follows.

(i) $\boldsymbol{\xi}_0(\phi) = [x(\phi), y(\phi), z(\phi)]$ defines the centreline trajectory of a closed double loop over $\phi = [1 : 4\pi]$ with $a = 0.5$, $w = 1.5$, a characteristic size of $r_f = 2$ and a perturbation of $r_1 = 0.25$.

$$\begin{array}{rrl} & x(\phi) = & r(\phi)\cos(\alpha), \\ & y(\phi) = & r(\phi)\sin(\alpha), \qquad z(\phi) = a\cos(\alpha), \\ \text{where} & r(\phi) = & r_f + r_1 a\cos(\phi) + a\sin(w\phi + \phi_0) \\ \text{and} & \alpha = & \phi + a\cos(w\phi + \phi_0)/(wr_f) \\ \text{with} & t_{NL} = & r_f^2/\Gamma = 8 \text{ the nonlinear time scale} \\ \text{and} & r_e = & (\Gamma/(\pi\omega_m))^{1/2} \text{ the effective radius.} \end{array} \tag{1.23}$$

(ii) The vorticity profile $|\omega(\rho)|$ uses the distance ρ between a given mesh point $\boldsymbol{x}$ and the nearest point on the trajectory $\boldsymbol{\xi}_0(\phi)$: $\rho = |\boldsymbol{x} - \boldsymbol{\xi}_0(\phi)|$. The profile used here is algebraic

$$\omega_{raw}(\rho) = \omega_o \frac{\left(r_o^2\right)^{p_r}}{\left(\rho^2 + r_o^2\right)^{p_r}} \tag{1.24}$$

for $\rho < \rho_+$, with a power-law of $p_r = 1$, a radius of $r_o = 0.25$ and a centreline vorticity before projection of $\omega_o \approx 1.26$. This profile is mapped onto the Cartesian mesh, is made incompressible as described previously (Kerr 2018*a*), and for algebraic profiles, the $\rho < \rho_+$ map is independent of the outer ρ_+ radius (Kerr 2023). The final ω_o is chosen in each case so that the circulation is always $\Gamma = 0.505$ (1.10) and $\|\omega(0)\|_\infty = 1$, with the initial enstrophy $Z_0 = Z(t = 0) \approx 5.30$.

All of the calculations in this paper use this initial condition with different domain sizes and different mesh sizes as given in table 1, including the curves in figures 2–5.

To demonstrate that this initial condition is compact, figure 1(*a*) shows the $r_1 = 0.25$ perturbed trefoil initial condition (1.23), with several paths being taken from the centre of

https://doi.org/10.1017/jfm.2025.10513 Published online by Cambridge University Press

the trefoil, through its initial trajectory, and out to the periodic boundaries. Additionally, figure 1(*b*) shows the vorticities $|\omega|$ and velocities $|u|$ along those paths. Both fields decay exponentially as they move out from the trefoil, with the velocity field flattening as the periodic boundaries are reached at $x = \pm 3\pi \approx 9.4$ and $y = \pm 3\pi \approx 9.4$, where one expects $\mathrm{d}|u|/\mathrm{d}s \sim 0$.

Furthermore, when each initial condition was set up, cross-sections were taken through the trefoil loops as they passed through these sets of half-mid-planes: for $y = 0$, $\big((x \gtrless 0) : (z \gtrless 0)\big)$ and for $x = 0$, $\big((y \gtrless 0) : (z \gtrless 0)\big)$, similar to what is shown in figure 7(*a*) of Kerr (2023). When the $(z \gtrless 0)$ pairs were added, the circulation through each of the $x \gtrless 0$, $y \gtrless 0$ pairs was $\pm 2\Gamma$, independent of size of the domain. Additionally, when the circulations of the half-planes were added, the net circulations over the full x:z and y:z mid-planes were zero.

The numerical method is the high-wavenumber filtered 2/3rds-dealiased pseudo-spectral code used previously (Kerr 2013*a*). However, by filtering out the ubiquitous high-wavenumer tail-up, one loses a simple tool for determining whether the smallest scales are resolved by observing that tail-up.

So alternative resolution diagnostics are needed. Comparisons between calculations with different resolutions is one choice and has been applied to the $\nu = 6.25 \times 10^{-5}$ calculations, with all of the $\Omega_m(t)$ moments for both 1024^3 calculations, that is, for both $(4\pi)^3$ and $(6\pi)^3$, agreeing with those of the 2048^3, $(4\pi)^3$ calculation.

For larger Reynolds numbers, whether the resolution is adequate is determined by these two diagnostics: behaviour of $\nu^{1/4}\mathcal{O}_{Vm}(t)$ and high-wavenumber k enstrophy spectra $Z_V(k)$ (3.1). Specifically, how well do the higher-order $\nu^{1/4}\mathcal{O}_{Vm}(t)$ moments in § 2.2 converge at their respective t_m times, as in figure 4? And from the $Z_V(k_x)$ spectra as in figure 9(*d*), do the $Z_V(k) \sim k_x^{-1}$ power laws bend into viscous exponential regimes?

Based upon those diagnostics, for the first factor of 25 decrease in ν, the small-scales of all of the intermediate ν, 1024^3 calculations and 2048^3 calculations to $\nu = 2.2 \times 10^{-5}$ are resolved for all times. This includes the § 4 graphics from the $\nu = 3.125 \times 10^{-5}$ calculation with the higher vorticity isosurfaces during reconnnection ($t = 42$ and 48) showing vortices curling around local pathways originating from the vicinity of the maximum vorticity ω_m.

Nonetheless, enstrophy based results for some larger Reynolds numbers with $\nu < 2.2 \times 10^{-5}$ calculations are included. For very early times, the convergences of $\nu^{1/4}\Omega_\infty(t)$ and $\nu^{1/4}\mathcal{O}_{V9}(t)$ are at $t_\infty = 18.4$ and $t_9 = 19.1$, respectively, for all ν are shown in figure 4, providing a clear sign that these $\nu < 2.2 \times 10^{-5}$ calculations are resolved for $t \lesssim 20$. Results for the enstrophy $Z(t)$ and $\mathcal{O}_{V1}(t)$ from three smaller ν calculations in large meshes are included in figures 2(*b*) and 6. These are for $\nu = 1.56 \times 10^{-5}$, 7.8×10^{-6} and 4×10^{-6}. They are included in the sense of large-eddy simulations, with the filtering smoothing the strongest grid-scale fluctuations. One justification is that all of the previous (Kerr 2018*b*) results using 1024^3 meshes have now been confirmed using 2048^3 meshes, implying that the same should be true for at least the new $\nu = 1.56 \times 10^{-5}$ and $\nu = 7.8 \times 10^{-6}$, 2048^3 results when re-run on 4096^3 meshes.

2. Vorticity moment scaling with powers of the viscosity ν

Figure 2 introduces the unexpected (circa 2018) convergence of $\sqrt{\nu}Z(t)$ (1.15), a reconnection-enstrophy. With $\ell > 1$, larger $(2\ell\pi)^3 > (2\pi)^3$ domains are used to ensure that temporal convergence at a fixed time $t_x \approx 40$ continues as the viscosity ν decreases. Using $\mathcal{O}_{V1}$ (1.1), Kerr (2018*a*) found that the best way to observe this convergence was to

https://doi.org/10.1017/jfm.2025.10513 Published online by Cambridge University Press

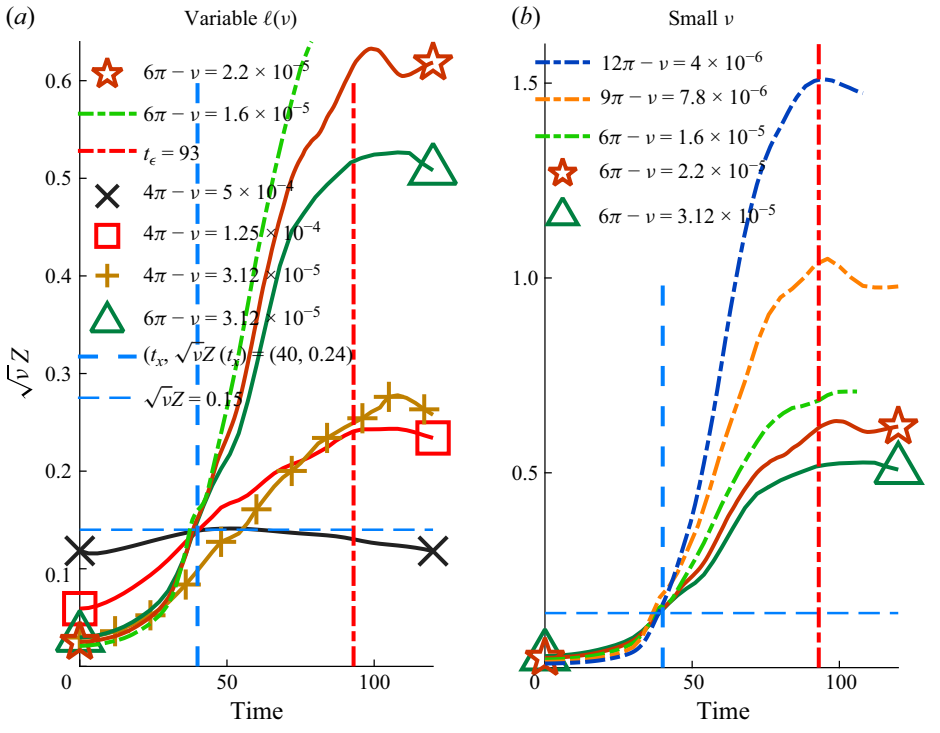


Figure 2. Time evolution of the reconnection enstrophy $\sqrt{\nu}Z(t)$ with all but one crossing at $t = t_x = 40$ with $\sqrt{\nu}Z(t_x) = 0.14$. The lower $\nu \leqslant 3.125 \times 10^{-5}$ viscous cases were given previously (Kerr 2018*b*) with $t_x = 40$ identified as the end of the reconnection phase. The line at $t = 93 \sim t_\epsilon$ is when plots of the dissipation $\epsilon = \nu Z$ approximately cross in figure 6. (*a*) The brown + curve is from $\nu = 3.125 \times 10^{-5}$, $(4\pi)^3$ calculations, the same domains as the lower $\nu < 3.125 \times 10^{-5}$ viscous cases, but $\sqrt{\nu}Z(t = 40) \neq 0.14$. Unlike the $\nu = 3.125 \times 10^{-5}$ green curve that was run in a $(6\pi)^3$ domain, with $\sqrt{\nu}Z(40) = 0.14$, plus a resolved $\nu = 2.2 \times 10^{-5}$ case (dark-red ⋆). (*b*) Along with the two highest Reynolds number $(6\pi)^3$, resolved calculations, $\nu = 3.125 \times 10^{-5}$ (green-triangle) and $\nu = 2.21 \times 10^{-5}$ (dark-red ⋆), three under-resolved higher Reynolds number, $\nu < 2.21 \times 10^{-5}$ cases show continuing convergence of $\sqrt{\nu}Z(t)$ at $t = t_x = 40$ as well as strong peaks at $t_\epsilon \approx 93 \approx 2t_x$. $t = 0$ for $(9\pi)^3 = (3 \times 3\pi)^3$ is slightly different as its $\sqrt{\nu}Z(t_x)$.

plot $B_\nu(t) = (\nu^{1/4}\mathcal{O}_{V1})^{-1} = 1/(\sqrt{\nu}Z(t))^{1/2}$ (1.15), discussed here in § 2.1 where $t_x \approx 40$ is taken to be when the reconnection phase ends, as defined by the figures in § 4.

In 2018, it was noted that the ν-independent convergence of $\sqrt{\nu}Z(t)$ seemed contrary to an analytic result from Constantin (1986). Kerr (2018*b*) suggested that an analytic extension of that old result might exist, which is now described in Appendix A.

Two simulations with $\nu = 3.1 \times 10^{-5}$ in figure 2 illustrate what happens if the domain is not increased as ν decreases. The brown + curve, done in a $\ell = 2$, $(4\pi)^3$ domain passes below $\sqrt{\nu}Z = 0.15$ at $t = 40$. The green △ curve was done in a $\ell = 3$, $(6\pi)^3$ domain and passes through $\sqrt{\nu}Z = 0.15$ at $t = 40$, which implies that in a $(4\pi)^3$ domain, the empirical critical viscosity for this initial condition is $\nu_c \sim 3.1 \times 10^{-5}$.

To maintain the $\sqrt{\nu}Z(t)$ convergence as the viscosity ν is decreased and the Reynolds number is increased further, ν_c had to be decreased by increasing the domain parameter ℓ repeatedly (Kerr 2018*a*,*b*). This practice was continued several times, showing empirically that the critical length scale ℓ_c depends upon ν as, or critical viscosity ν_c depending upon the length scale ℓ as

$$\ell_c \sim \nu^{-1/4} \quad \text{or} \quad \nu_c \sim \ell^{-4}. \tag{2.1}$$

https://doi.org/10.1017/jfm.2025.10513 Published online by Cambridge University Press

This raises the question: what is the origin of the dependence of the empirical critical viscosities $\nu_c(\ell)$ upon ℓ and $\nu^{-1/4}$? Section 2.2 discusses the ubiquitous nature of the $\nu^{1/4}$ scaling, with the appearance of double vortex sheets in § 4 seeming to underly the dynamics. However, trefoils are too complicated to be able to see the underlying dynamics clearly, so alternative configurations such as orthogonal vortices are being used, with the preliminary conclusion summarised in § 6 as folllows.

(i) The usual $\sqrt{\nu}$ scaling does appears as the double sheets are being pushed together.
(ii) This is balanced by $\ell \sim \nu^{-1/4} = (\sqrt{\nu})^{-1/2}$ scaling developing at their outer edges as the sheets spread out.

Note that the convergence of $\sqrt{\nu}Z(t)$ as ν decreases is not convergence of the energy dissipation rate $\epsilon = \nu Z$, which comes later, for $t > t_x$, as the post-reconnection enstrophy growth accelerates. Unlike the similarity-like growth of the higher-order vorticity moments described next, similar convergence of $\epsilon(t) = \nu Z$, around a given time, should not be expected. Instead, there is approximate convergence of $\epsilon(t) = \nu Z$ that begins at $t \sim 70$ with peaks at $t_\epsilon \approx 2t_x \sim 93$ in figure 6, with associated spectra that are discussed in § 3.

2.1. *Reconnection phase scaling* $(\sqrt{\nu}Z)^{-1/2} = (\nu^{1/4}\mathcal{O}_{V1})^{-1}$

In this subsection, figure 3(*a*) uses this viscous rescaling of $Z(t)$ (Kerr 2018*b*), $B_\nu(t) = 1/(\sqrt{\nu}Z(t))^{1/2} = (\nu^{1/4}\mathcal{O}_{V1})^{-1}$ (1.15), while figure 3(*b*) introduces scaling of the dissipation rate $\epsilon = \nu Z$ (1.12) that is covered more throughly in figure 6 when enstrophy spectra are discussed.

Since originally introduced by Kerr (2018*a*, 2018*b*), convergent, inverse linear $B_\nu(t)$ regimes have been found for the interaction of coiled vortex rings (Kerr 2018*c*), three-fold symmetric trefoils (Kerr 2023) and additional configurations discussed in § 5.1.

The extensions in figure 3(*a*) come from linearising $B_\nu(t)$ about ν-independent $B_x = B_\nu(t_x) \approx 2.67$ for $t \lesssim t_x$ $(30 \leqslant t \leqslant 40)$ and extending each linear $B_\nu(t)$ to $T_c(\nu) > t_x$, when $t > t_x$ inverse linear ends with $B_\nu(T_c(\nu)) = 0$.

Specifically, for $t_{30} = 30$ and $t_x = 40$, one gets the $\Delta t(\nu)$ and $T_{c1}(\nu)$ in figure 3(*a*,*c*) using

$$\Delta t(\nu) = B_x \frac{t_x - t_{30}}{B_\nu(t_{30}) - B_x} \quad \text{and} \quad T_{c1}(\nu) = t_x + \Delta t(\nu). \tag{2.2}$$

The purpose of identifying these $t > t_x$ linear extensions is to emphasise the inverse linearity of the pre-t_x $B_\nu(t)$, which suggests some type of self-similar process might be found. Figure 3(*c*) shows that $\Delta t(\nu)$ decreases significantly as ν decreases.

These observations suggest that an underlying scaling process exists with a role for the double square-root on the viscosity, that is, when scaled using $\nu^{1/4}$ (1.15). The next section will follow this up by extending the $\nu^{-1/4}\mathcal{O}_{V1}^{-1}$ scaling to higher order $\mathcal{O}_{Vm}$ and § 6 will begin by mentioning other configurations with this scaling.

2.2. *Additional* $\nu^{1/4}$ *scaling examples*

Figure 4 shows inverse $\nu^{1/4}$ scaling of $\Omega_\infty(t)$ and $\mathcal{O}_{V9}(t)$ (1.1): $(\nu^{1/4}\Omega_\infty(t))^{-1}$ and $\left(\nu^{1/4}\mathcal{O}_{V9}(t)\right)^{-1}$, recalling that at $t = 0$, $\Omega_\infty = \|\omega\|_\infty = 1$ is imposed. For all m, the $\nu \leqslant 6.25 \times 10^{-5}$ cases have the best temporal convergence, with the larger ν cases gradually joining those convergences as m decreases.

Figure 4(*a*) shows that the ν-independent temporal convergence of $(\nu^{1/4}\Omega_\infty(t))^{-1}$ is at $t_\infty = 18.4$ and figure 4(*b*) shows this for $\left(\nu^{1/4}\mathcal{O}_{V9}(t)\right)^{-1}$ at $t_9 = 19.1$. For both, there are

https://doi.org/10.1017/jfm.2025.10513 Published online by Cambridge University Press

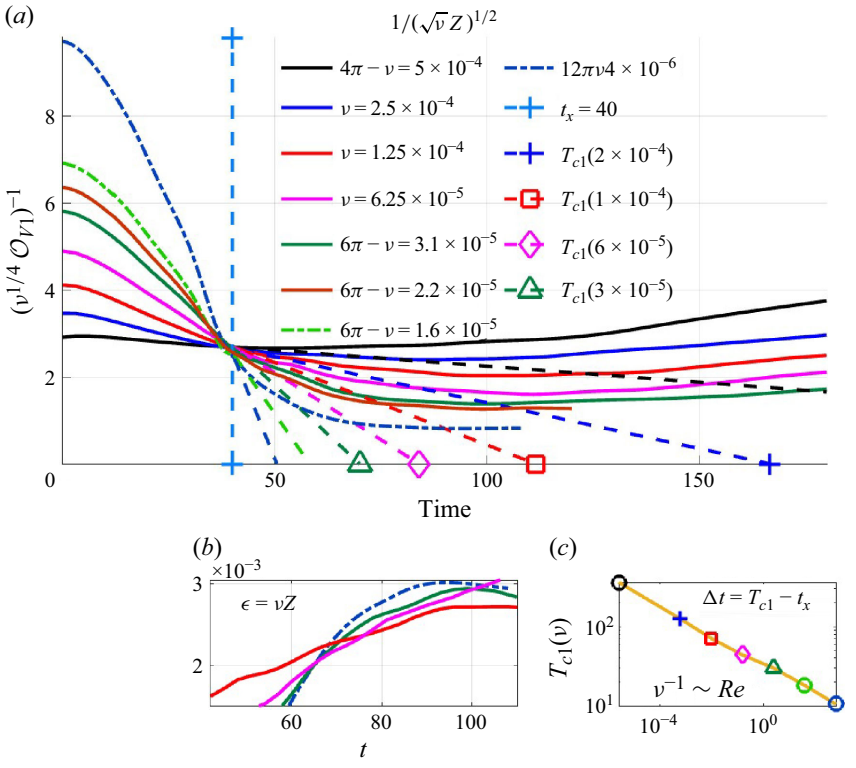


Figure 3. Panel (*a*) and inset (*b*) show further viscosity-based rescalings of the enstrophy Z. (*a*) Inverse $(\sqrt{\nu}Z)^{-1/2}$ scaling, rewritten as $(\nu^{1/4}\mathcal{O}_{V1})^{-1}$. This shows ν-independent inverse-linear convergence at $t = t_x = 40$. To emphasise that the convergence is inverse linear, $t > t_x$ extensions of the $t \lesssim t_x$ behaviour are shown using long dashed lines. The linear $t \lesssim t_x$ sections are determined by local $[364 \geqslant \Delta t(\nu) \geqslant 10.5]$ (2.2), plotted in panel (*c*), which then give the $T_c(\nu)$ (2.2) extensions. (*b*) Dissipation rates $\epsilon = \nu Z(t)$ for a few viscosities, with the same time axis as in panel (*a*), with the complete $\epsilon(t)$ curves given in figure 6.

temporal convergences at t_∞ and t_9 for $\nu = 6.25 \times 10^{-5}$ to 4×10^{-6}. For the dash-dotted $\nu < 1.56 \times 10^{-5}$ cases, the resolution is adequate only up to $t \sim 19$, but inadequate after that for the highest-order moments. The lower Reynolds number $\nu = 1.25 \times 10^{-4}$ curves at t_∞ and t_9 have smaller $(\nu^{1/4}\Omega_m(t))^{-1}$, larger $\nu^{1/4}\mathcal{O}_{Vm}(t)$, consistent with their temporal convergences tending to be slightly later, as seen for $m = 4$ in the next figure.

The convergences of these large m, $\nu^{1/4}\mathcal{O}_{Vm}$, provide the earliest quantitative evidence that the size of the domain is affecting vorticity growth. That is, a sign that the local growth of $\Omega_\infty = \|\omega\|_\infty$ (and $\mathcal{O}_{V9}$) is being affected by interactions across the periodic boundaries, interactions that can be suppressed if the periodic domains are increased as $\ell \sim \nu^{-1/4}$ as ν decreases. The $t \lesssim t_m$ evolution of all the $\left(\nu^{1/4}\mathcal{O}_{Vm}(t)\right)^{-1}$ are approximately inverse-linear, similar to how $(\nu^{1/4}\mathcal{O}_{V1}(t))^{-1}$ behaves in figure 3. Note that both t_∞ and t_9 are at $\approx t_x/2$.

Can this early time evolution of $\nu^{1/4}\Omega_\infty(t)$ and $\nu^{1/4}\mathcal{O}_{V9}(t)$ tell us anything about the origins of the $\nu^{1/4}$ scaling? For that, a physical model will be needed that takes into account the origin, extent and scaling of vortex sheets like those in figures 11 and 12. However, first, let us consider the evolution of the intermediate vorticity moments, $\mathcal{O}_{Vm}(t)$.

For all orders m, there is convergence of almost all the $\nu^{-1/4}\mathcal{O}_{Vm}^{-1}$ at their respective t_m, ordered as $t_\infty < \ldots < t_m \ldots t_1 = t_x$, with ν-independent $\sqrt{\nu}Z(t_x)$ above all others.

https://doi.org/10.1017/jfm.2025.10513 Published online by Cambridge University Press

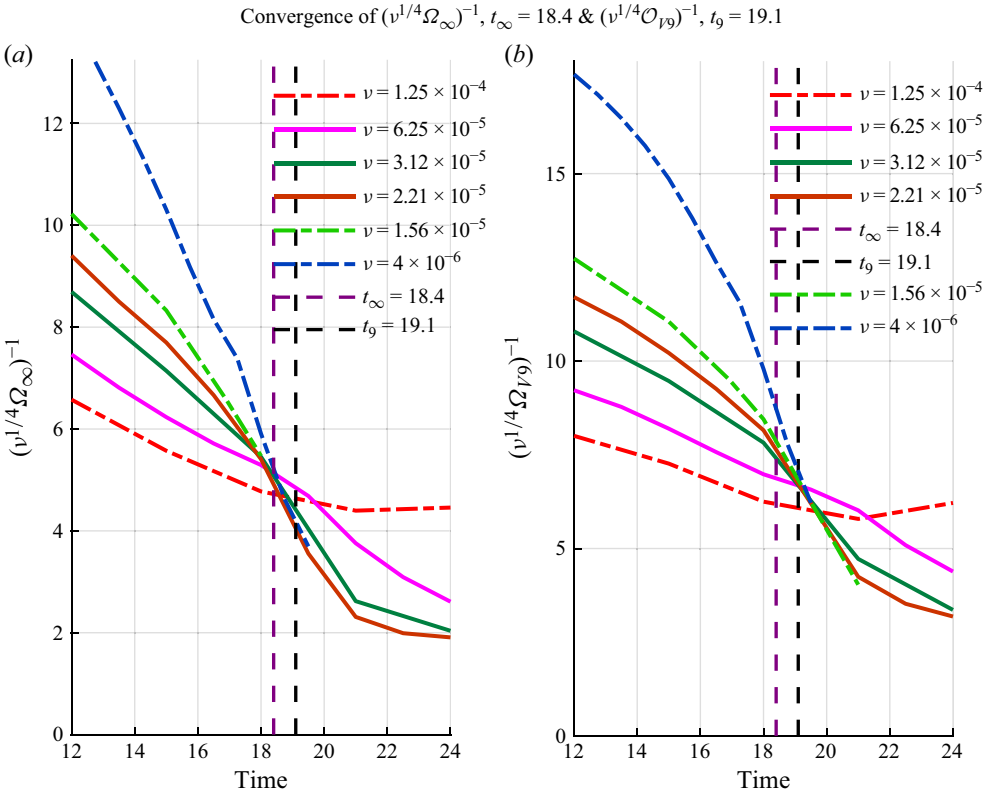


Figure 4. (*a*) $(\nu^{1/4}\Omega_\infty)^{-1}$ and (*b*) $(\nu^{1/4}\mathcal{O}_{V9})^{-1}$ with (1.9) showing how each $\mathcal{O}_{V9}$ is bounded by $V_\ell^{1/2m}\Omega_\infty$ (1.9). Outliers, indicated by dash-dotted lines, are under-resolved $\nu < 2.21 \times 10^{-5}$ and a delayed crossing for $\nu = 1.25 \times 10^{-4}$. Recall that the end of the reconnection phase is indicated by when the $\sqrt{\nu}Z(t)$ converge at $t_x = 40$ in figure 3. For $\nu = 6.25 \times 10^{-5}$ to $\nu = 4 \times 10^{-6}$, in panel (*a*), the $(\nu^{1/4}\Omega_\infty(t))^{-1}$ converge at $t_\infty \sim 18.4$ and in panel (*b*), the $(\nu^{1/4}\mathcal{O}_{V9})^{-1}$ converge at $t_9 \sim 19.1$.

Figure 5 shows two of these intermediate scaled, inverse moments. Here, $\nu^{-1/4}\mathcal{O}_{V4}^{-1}$ and $\nu^{-1/4}\mathcal{O}_{V2}^{-1}$. For $\nu^{-1/4}\mathcal{O}_{V4}^{-1}$ from $\nu = 6.25 \times 10^{-5}$ to $\nu = 1.56 \times 10^{-5}$, there is convergence at $t_4 = 22$ and for $\nu^{-1/4}\mathcal{O}_{V2}^{-1}$ for the same ν at $t_2 = 29.3$.

One way to understand the relationship between $\nu^{1/4}\Omega_\infty$ and the $m < \infty$ volume-integrated moments $\nu^{1/4}\mathcal{O}_{Vm}(t)$, including the $(\sqrt{\nu}Z)^{1/2} = (\nu^{1/4}\mathcal{O}_{V1})^2$, is to realise that $\|\omega\|_\infty = \Omega_\infty$ is point-like. Because the $t_\infty = 18.4$ convergence comes first, as ω near $\Omega_\infty(t)$ continues to grow, the region with $\omega \sim \|\omega\|_\infty$ begins to spread out, resulting in increases of the other $\mathcal{O}_{Vm}$, until one gets vortex sheets like those in figure 11.

To determine whether the resolution is adequate, one common diagnostic is to follow and compare values of $\|\omega\|_\infty = \Omega_\infty$, with figure 4 showing both $\nu^{1/4}\Omega_\infty(t)$ and $\nu^{1/4}\mathcal{O}_{V9}(t)$ converging at $t_\infty = 18.9$ and $t_9 = 19.1$, respectively, for all ν. Furthermore, for $\nu \gtrsim 2.2 \times 10^{-5}$ and $t \geqslant 20$, as ν decreases, the inverse $\|\omega(t)\|_\infty$ and $\mathcal{O}_{V9}(t)$ continue to decrease as expected.

However, for $t > 20$, the smaller ν, $\nu < 2.2 \times 10^{-5}$, the highest-order Ω_m do not decrease as would be expected, indicating that they are no longer fully resolved and are not shown, which leads to the conclusion that the only calculations that are adequately resolved for all times are those with $\nu \geqslant 2.21 \times 10^{-5}$, which is 1/25 of $\max(\nu) = 5 \times 10^{-4}$.

https://doi.org/10.1017/jfm.2025.10513 Published online by Cambridge University Press

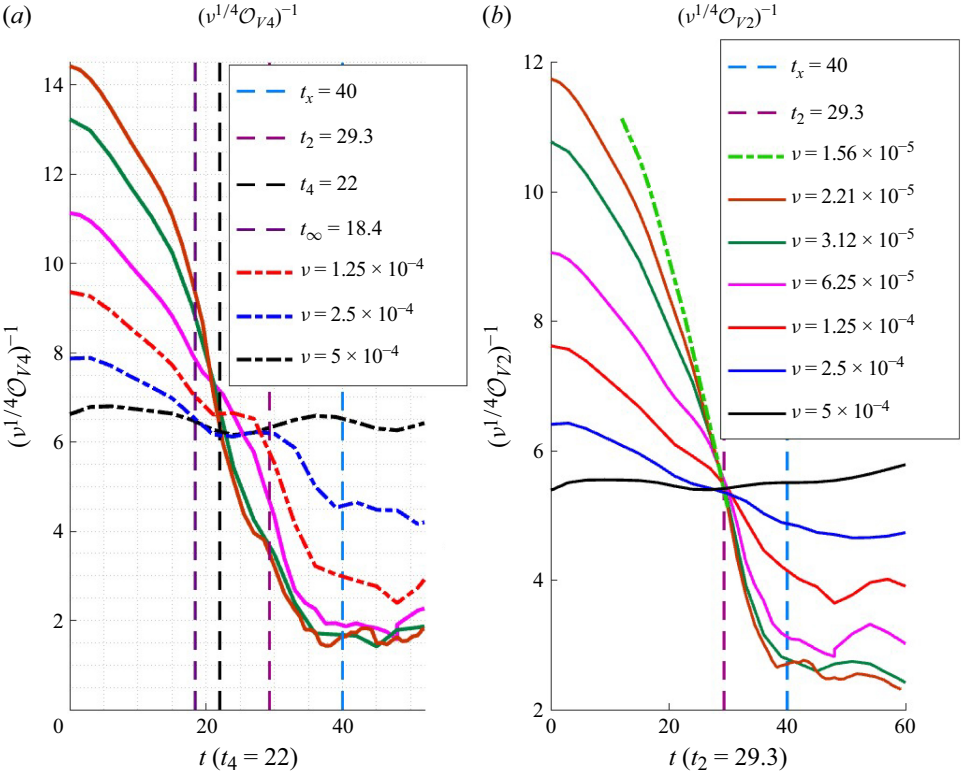


Figure 5. $\nu^{1/4}\mathcal{O}_{Vm}$ for $m = 2, 4$. Right legend shows the colours for all the ν plotted in both frames. Both frames show $t_1 = t_x = 40$, the end of the reconnection phase, and $t_2 = 29.3$. (*a*) $\nu^{1/4}\mathcal{O}_{V4}$ for $t \leqslant 50$. Also marked are $t_4 \sim 22$ and $t_\infty \sim 18.4$ with $t_x > t_2 > t_4 > t_\infty$. For $\nu \leqslant 6.25 \times 10^{-5}$, the $\nu^{1/4}\mathcal{O}_{V4}(t)$ converge at t_4 and for $\nu \geqslant 1.25 \times 10^{-4}$ in $-\cdot$, the convergence is around t_2 (*b*) All $\nu^{1/4}\mathcal{O}_{V2}$ for $t \leqslant 60$, including $\nu = 1.56 \times 10^{-5}$, converge at $t_2 = 29.3$.

3. Dissipation and spectra

The convergence properties of the $\nu^{-1/4}\mathcal{O}_m(t)$ scaled vorticity moments just reported come from a phase when the dynamics is dominated by the emergence of $h < 0$ vortex sheets, which might be indicating the emergence of a self-similar process. Can this scaling be extended to cover convergence of the dissipation rates $\epsilon(t)$?

It would be surprising if for $t \geqslant t_x \sim 40$, after reconnection begins, whether $(\nu^{1/4})^2$ enstrophy and dissipation rate scaling would continue, which it does not, as $\epsilon(t) = \nu Z(t) = (\sqrt{\nu}\mathcal{O}_{V1})^2$ in figure 6 shows for $t \geqslant 40$. Nonetheless, the set of $\epsilon(t) = \nu Z(t)$ curves in figure 6 do indicate that the growth of the post-reconnection enstrophy accelerates sufficiently to obtain good convergence of $\epsilon(t)$ at $t \sim 70$ for $\nu \leqslant 1.25 \times^{-5}$, with $t > 70$ approximate convergence through the maxima at $t_\epsilon \sim 93 \sim 2t_x$ and continuing to $t \sim 180$. This means large $\epsilon(t)$ for a period of at least $\Delta T_\epsilon \sim 2t_x \searrow t_\epsilon$ at the end of these calculations, observed both here and for the three-fold symmetric trefoils (Kerr 2023). These observations provide evidence for finite ΔE_ϵ (1.2) and satisfy one definition for a dissipation anomaly with finite-time integrated energy dissipation.

Is this variation in $\epsilon(t)$ compatible with experimental observations? A recent set of experiments shows that the dissipation coefficient C_ϵ (1.3) behind bluff bodies has a variation of approximately 20 % around $C_\epsilon \sim 0.25$ (1.3) (Schmitt *et al.* 2024), similar to

https://doi.org/10.1017/jfm.2025.10513 Published online by Cambridge University Press

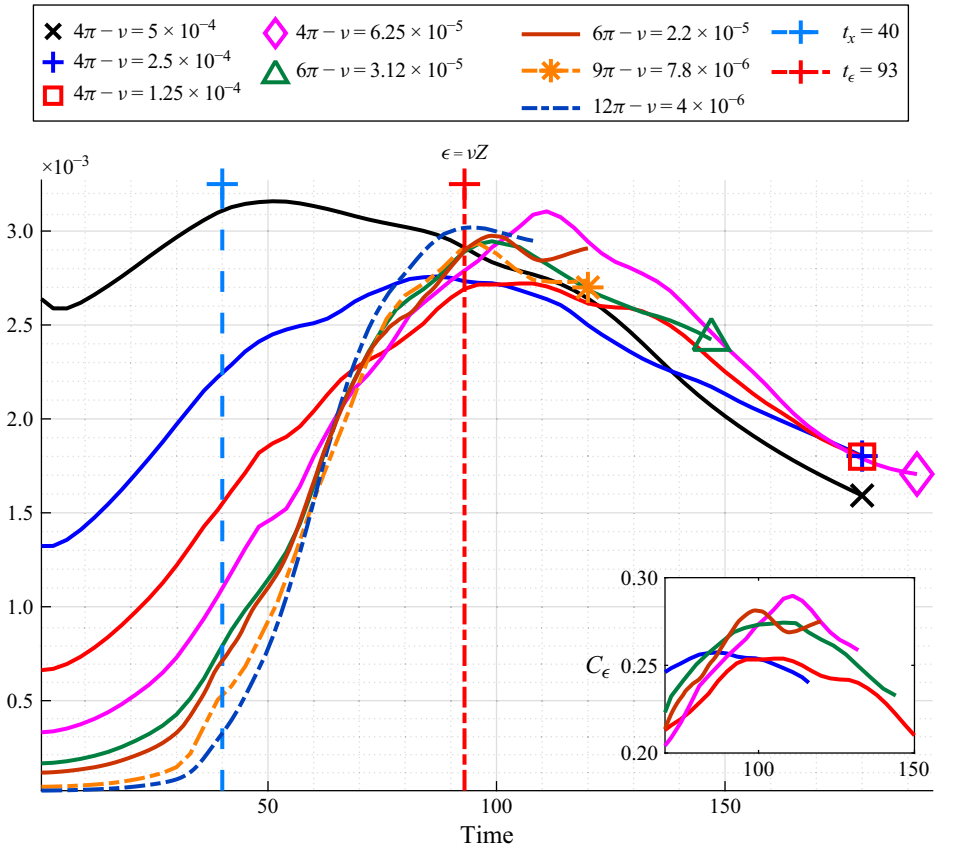


Figure 6. Dissipation rate $\epsilon = \nu Z$ for seven cases, $\nu = 5 \times 10^{-4}$ to 4×10^{-6}, showing approximate convergence of the dissipation rates beginning at $t \sim 70$ for $\nu \leqslant 1.25 \times^{-5}$, with peaks at $t_\epsilon \approx 93 \approx 2t_x$ that continue for an extended period. These trends are consistent with the formation of a dissipation anomaly, that is, finite energy dissipation ΔE_ϵ (1.2) in a finite time as ν decreases. Inset: ϵ rescaled as the dissipation coefficient C_ϵ (1.3) using $\mathcal{L} = 2r_f = 4$ and $\mathcal{U} = \|u\|_\infty(t_\epsilon = 93) \approx 0.34$ for calculations whose maximum Taylor microscale Reynolds number at $t = 93$ is $R_\lambda = 218$.

what is shown in the inset of figure 6, rather than the larger C_ϵ values from older wind tunnel experiments (Vassilicos 2015).

The experiments go further and suggest that the configuration dependence is related to intermittency coefficient μ, a structure function property beyond the scope of these simulations.

However, instead of structure functions, the evolution of wavenumber spectra can be followed and one can ask: how do the enstrophy spectra $Z_V(k, t)$ (3.1), another measure of the dissipation, behave over this time span?

3.1. *Enstrophy spectra and production*

One set of tools that can demonstrate how the energy and enstrophy go from large to small scales is their spectra, complemented by their spectral transfer and production spectra.

Energy spectra $E_V(k, t)$ are formed by taking Fourier transforms of the velocity (1.17) and enstrophy spectra $Z_V(k, t)$ are formed with the vorticity $\boldsymbol{\omega}$ replacing the velocity $\boldsymbol{u}$ in

https://doi.org/10.1017/jfm.2025.10513 Published online by Cambridge University Press

the Fourier transforms. Using (1.20), these are

$$E_V(k,t)=\frac{1}{2}\sum_{\boldsymbol{k}}|\hat{\boldsymbol{u}}_{\boldsymbol{k}}(t)|^2 \quad \text{and} \quad Z_V(k,t)=\sum_{\boldsymbol{k}}|\hat{\boldsymbol{\omega}}_{\boldsymbol{k}}(t)|^2. \tag{3.1}$$

The types of sums taken depend upon the definition of k. If k is in one of the three wavenumber directions k_x, k_y and k_z, the sums are taken over the two perpendicular directions. In this paper, all spectra use three-dimensional wavenumbers

$$k=|\boldsymbol{k}|=\sqrt{k_x^2+k_y^2+k_z^2}\,, \tag{3.2}$$

with $E_V(k,t)$ and $Z_V(k,t)$ collected in wavenumber shells $\mathbb{Z}/\ell\leqslant k<\mathbb{Z}+1$ whose element-numbers for small k are discontinuous, which can lead to ambiguities (Kerr 1990). The wavenumbers of the shells are the mean-square averages of the wavenumbers within them. For the variable $(2\ell\pi)^3$ domains in this paper, there are minimum wavenumbers k_{min} such that all $\boldsymbol{k}$ obey

$$|\boldsymbol{k}|\geqslant k_{min}=\min_{k\neq 0}(k)=1/\ell=1/3. \tag{3.3}$$

The spectral equation for $E_V(k,t)$ is

$$\frac{\mathrm{d}}{\mathrm{d}t}E_V(k,t)=T(k)-\nu Z_V(k,t), \tag{3.4}$$

with the integral of the energy-transfer identically zero: $\int T(k)\,\mathrm{d}k\equiv 0$. The spectral equation for the enstrophy is similar, with non-zero enstrophy production ζ_p replacing the energy transfer,

$$\frac{\mathrm{d}}{\mathrm{d}t}Z_V(k,t)=\zeta_p(k)-2\nu P_V(k,t), \tag{3.5}$$

with $\zeta_p(k)$ being the Fourier transform of the physical space enstrophy density production $\zeta_p(\boldsymbol{x},t)=2\boldsymbol{\omega}\boldsymbol{S}\boldsymbol{\omega}$ (1.13) and $P_V(k,t)$ being the palinstrophy, which at individual wavenumbers $\boldsymbol{k}$ is $P_V(\boldsymbol{k},t)=\boldsymbol{k}^2Z_V(\boldsymbol{k},t)=2\boldsymbol{k}^4E_V(\boldsymbol{k},t)$ with $P_V(k,t)\approx 2k^4E_V(k,t)$. The $\zeta_p(\boldsymbol{k})$ are determined numerically at run-time by Fourier transforming the vortex stretching term $\boldsymbol{S}\boldsymbol{\omega}$ and the enstrophy $\boldsymbol{\omega}$ simultaneously, then multiplying $\widetilde{\{\boldsymbol{S}\cdot\boldsymbol{\omega}\}}(\boldsymbol{k})$ and $\boldsymbol{\omega}(\boldsymbol{k})$ in Fourier space, with $\widetilde{\{\,\}}$ indicating a Fourier transform. This gives the following enstrophy production spectra and global enstrophy production in the enstrophy equation (1.13):

$$\zeta_p(k,t)=2\boldsymbol{\omega}(\boldsymbol{k})\cdot\widetilde{\{\boldsymbol{S}\cdot\boldsymbol{\omega}\}}(\boldsymbol{k})\approx 2k^2T(k)$$
$$\text{and}\quad Z_p(t)=\int \mathrm{d}k\;\zeta_p(k,t)=\int_{\mathcal{V}_\ell}2\boldsymbol{\omega}\boldsymbol{S}\boldsymbol{\omega}\,\mathrm{d}V. \tag{3.6}$$

The evolution of the dissipation rate $\epsilon(t)=\nu Z_p(t)$ and its nonlinear production $\nu Z(t)$ are given in figure 10 after the $Z_V(k,t)$ enstrophy spectra. The $T(k,t)$ and $\zeta_p(k,t)$ spectra are mentioned, but a full discussion will require another paper.

One numerical paradigm for representing turbulent states is homogeneous, isotropic turbulence generated by forcing the flow at small wavenumbers (large length scales). With statistically steady data from calculations run in large enough domains, these can generate $k^{-5/3}$ Kolmogorov spectra, starting with Kerr (1985) and since then, much higher Reynolds numbers (Ishihara, Gotoh & Kaneda 2009). One advantage that these statistically steady data sets have is that time averages can be taken that smooth out transients.

https://doi.org/10.1017/jfm.2025.10513 Published online by Cambridge University Press

Taking steady-state averages is less of an option for the transient flows generated from configurations of reconnecting vortices. Without statistically steady data that allow averaging over long times to get wavenumber scaling, transient energy spectra $E_V(k,t)$ and enstrophy spectra $Z_V(k,t)$ (3.1) can be followed through the wavenumber scales to indicate how the energy and enstrophy move, grow and decay through the wavenumbers and how energy dissipation rates, $\epsilon = \nu Z$, evolve through scales to generate finite-time dissipation. If a flow is believed to generate finite energy dissipation, or other signatures of turbulence, some transient $E_V(k,t) \sim k^{-5/3}$ spectra might develop, which for the enstrophy would be $Z_V(k,t) \sim k^{1/3}$.

The only Kolmogorov-like $E_V(k) \sim k^{-5/3}$ spectra from reconnection simulations are from anti-parallel cases. With a Gaussian profile, Yao & Hussain (2020) obtained $k^{-5/3}$ for a short time-span (see also Yao & Hussain 2022). Additionally, with an algebraic profile, Kerr (2013*a*) obtained $k_y^{-5/3}$ over a sustained time-span when normalised by time-varying $\epsilon^{2/3}$ as the the energy $E(t)$ decreases by 50 %. These are mentioned again at the end of § 5.2.

Only one Gaussian profile trefoil calculation reports spectra, with Yao *et al.* (2021) finding a $E_V(k) \sim k^{-7/3}$ regime that, like the Yao & Hussain (2020) inertial range, begins as high wavenumbers with very little associated energy dissipation.

3.2. *Algebraic trefoil spectra*

Could a trefoil vortex knot with an algebraic initial profile overcome the limitations of Yao *et al.* (2021) without taking ensemble averages? That is, can it generate finite energy dissipation and with Kolmogorov-like spectral scaling?

To facilitate comparisons over several viscosities, only an $\ell = 3$, $(6\pi)^3 = (2\ell\pi)^3$ domain is used for plotting three-dimensional enstrophy spectra $Z_V(k)$. The enstrophy spectra are used because under Kolmogorov scaling, the $Z_V(k)$ scale as $k^{1/3}$ $(= k^2 k^{-5/3})$, which can be easily recognised, unlike $E_V(k) \sim k^{-5/3}$ scaling, which requires plotting $k^{5/3} E_V(k)$ (Kerr 2013*a*).

To identify the significant temporal regimes, several plausible comparison power laws, $k^{1/3}$, k^{-1} and k^{-2}, are shown. Comparisons to these power laws are meant less for determining the particular subranges and more for showing what the spectra are not.

If $Z_V(k) \sim k^{1/3}$ is found, further questions might include whether $Z_V(k)$ overshoots $k^{1/3}$, whether there are brief $Z_V(k,t)$, sub-$k^{1/3}$ periods, how long $k^{1/3}$ scaling is maintained and then how $Z_V(k)$ dissipates. The extent of any brief Lundgren-like inertial subranges is given in terms of both k and k_{min} (3.3). Figure 7 shows the progression over $t = 0$ to $t = 120$ of $Z_V(k,t)$ for $2/3 \leqslant k \leqslant 33$ from the $\nu = 3.125 \times 10^{-5}$ calculation, with the following points.

(i) The spectra for $k < 2$ generally decrease with time.
(ii) At higher $k \geqslant 6 = 18 k_{min}$, there is a steady progression from the very steep $t = 0$ spectrum to $Z_V(k) \sim k^{-1}$ spectra (like $E_V(k) \sim k^{-3}$) that are discussed further using figure 9(*d*).
(iii) The $t = 36$ and $t = 48$ spectra overshoot the $k^{1/3}$ scaling for $k > 2$.
(iv) $t = 48$ is marked using a dash-dotted line because this represents the transition between pre- and post-reconnection scaling, after which $Z_V(k,t)$ spreads out in k until $t = 72$.
(v) $k^{1/3}$ scaling goes through both the $t = 72$ and $t = 80$ curves for $3 \leqslant k \leqslant 4$ $(9 \leqslant k/k_{min} \leqslant 12)$ in both figures 7 and 8(*a*), with the full $2 \leqslant k \leqslant 10$ behaviour in figure 8(*a*).

https://doi.org/10.1017/jfm.2025.10513 Published online by Cambridge University Press

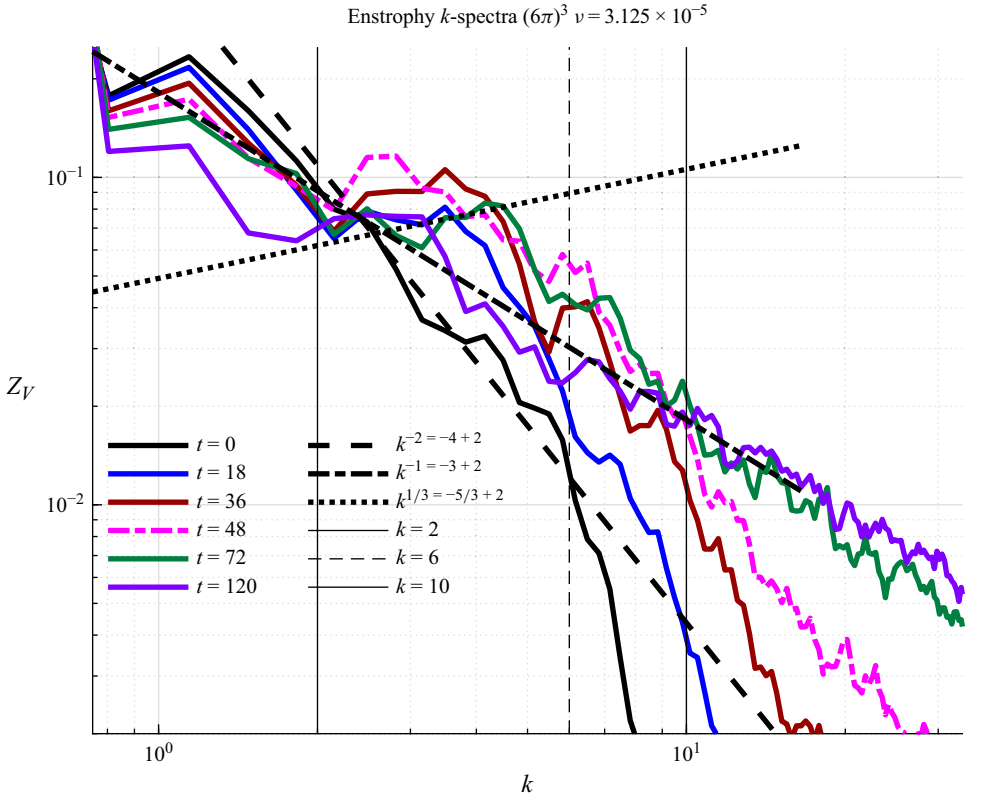


Figure 7. Enstrophy spectrum $Z_V(k, t)$ (3.1) for seven times from the $\nu = 3.125 \times 10^{-5}$ perturbed trefoil case run in a $(6\pi)^3$ domain. Times are $t = 6$, 18, 36, 48, 72, 96 and 120, plus three power laws, $k^{-5/3+2} = k^{1/3}$, $k^{-3+2} = k^{-1}$ and $k^{-4+2} = k^{-2}$. Due to the logarithmic k-scale, $k < 2$ values are over-emphasised compared with $k > 2$ values. The $Z_V(k, t) < 2$ spectra generally decrease with time as small-wavenumber energy begins to transfer to higher wavenumbers, with the exception of $k = 2$ at $t = 48$ as noted for figure 9(*b*). The $k \geqslant 6$ spectra gradually grow over time until all approximately obey k^{-1} for all $10 \leqslant k \leqslant 30$.

Figure 8 shows the progression of $Z_V(k, t)$ for two viscosities from $t = 0$ to $t = 92$ or 93 for $\nu = 3.125 \times 10^{-5}$ and $\nu = 6.25 \times 10^{-5}$, respectively. For both viscosities, for $2 < k < 4$, there is growth of $Z_V(k, t)$ for $t < 48$; for $k > 6$ over all times, as t increases, $Z_V(k, t) \sim k^{-1}$ regimes are forming. At intermediate $k \sim 2.5{-}3.5$, at both $t = 36$ and 48, there is overshooting of any developing $k^{1/3}$ scaling.

There are differences in whether $Z_V \sim k^{1/3}$ regimes are forming for the two Reynolds numbers in figure 8. For panel (*a*), $\nu = 3.125 \times 10^{-5}$ and $t = 72$, there is a $Z_V \sim k^{1/3}$ regime for $2 \leqslant k \leqslant 4$, which at $t = 80$, moves to $3 \leqslant k \leqslant 4.5$ ($9 \leqslant k/k_{min} \leqslant 13.5$).

The lower Reynolds number in figure 8(*b*) with $\nu = 6.25 \times 10^{-5}$ shows the $k \geqslant 2$ spectra increasing until $t = 48$, including a growing high-wavenumber $Z_V(k, t) \sim k^{-1}$ regime. However, the $k \gtrsim 3$ spectra never develop a convincing $Z_V \sim k^{1/3}$ and instead tend to decay, but not uniformly.

These observations raise the following questions.

(i) How does the approximately $Z_V(k) \sim k^{1/3}$ spectra scaling develop?
(ii) Does this spectrum persist long enough to attain finite energy dissipation ΔE_ϵ (1.2)?

https://doi.org/10.1017/jfm.2025.10513 Published online by Cambridge University Press

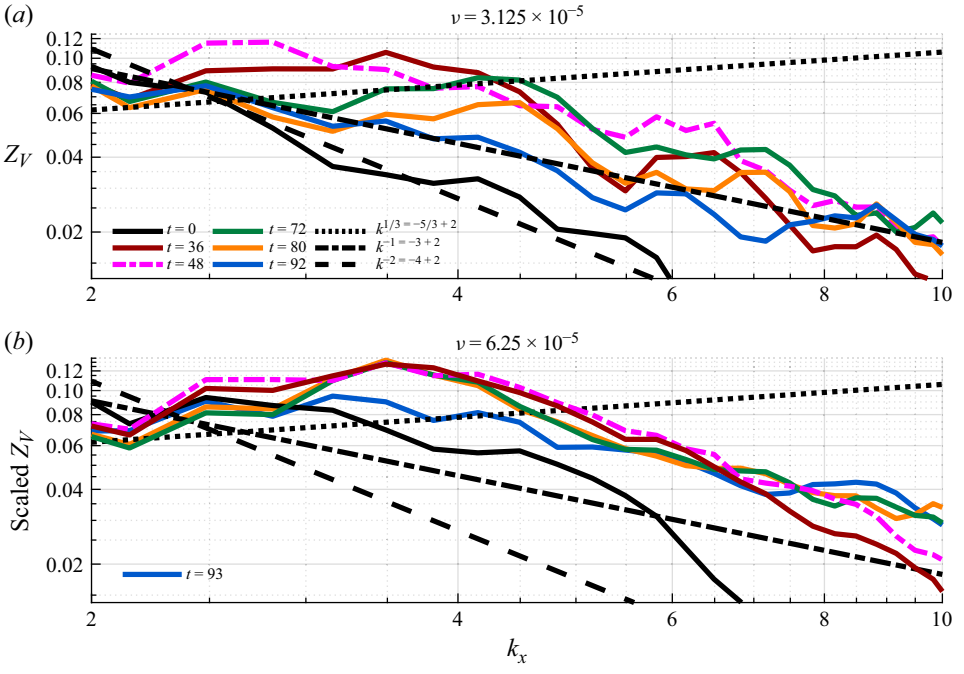


Figure 8. Comparisons of enstrophy spectra $Z_V(k, t)$ (3.1) for two intermediate resolved Reynolds number (Re) calculations at $t = 0$ and intermediate times ($t = 36$ to 92 or 93) for the wavenumber span $2 < k < 10$ to show the first step in how the enstrophy's form of Lundgren scaling, $Z_V(k) \sim k^{1/3}$, develops. For $\nu = 3.125 \times 10^{-5}$, panel ($a$) shows that at $t = 48$ for $k \sim 3$, the $Z_V(k, t)$ spectrum briefly overshoots $k^{1/3}$, before becoming $Z_V(k, t) \sim k^{1/3}$ for $t = 72$ to 80. For $\nu = 6.25 \times 10^{-5}$, panel ($b$) shows that for smaller Re, the spectrum also overshoots $k^{1/3}$, but a clear $Z_V(k, t) \sim k^{1/3}$ regime does not form afterwards.

To help answer those questions, figures 9 and 10 show enstrophy and enstrophy production spectra from the highest Reynolds number $\nu = 2.2 \times 10^{-5}$ resolved simulation. Figure 9 uses four time frames to show how a transient $Z_V(k, t) \sim k^{1/3}$ regime forms and how long it persists.

(i) Figure 9(a–c) all cover $2 \leqslant k \leqslant 6$ ($6 \leqslant k/k_{min} \leqslant 18$) as follows.
(ii) Figure 9(a) highlights the overshoot phase that ends between $t = 36$ and 48.
(iii) Figure 9(b) shows a settling phase with the best evidence for Lundgren-like $Z_V(k) \sim k^{1/3}$ scaling over a brief time span of $t = 66$ to $t = 78$ as the enstrophy spectrum settles over $2.67 \leqslant k \leqslant 4.33$, ($8 \leqslant k/k_{min} \leqslant 13$), with the peak of $Z_V(k > 3)$ moving to larger k as t increases. This span of times and wavenumbers provides the best evidence for how energy and enstrophy are moving to large k coherently.
(iv) Figure 9(c) covers times $t \sim 75-111$ within the temporal span of figure 6 with temporal convergence of the energy dissipation rates $\epsilon(t)$ (1.12) for several viscosities, with the maxima of the $\epsilon(t)$ at $t_\epsilon \approx 93$.
(v) Over this time span, the higher wavenumbers gradually decay from $k^{1/3}$ to k^{-1} due to high wavenumber dissipation.
(vi) Figure 9(d) shows both (1) very low $k \leqslant 2$ in the inset and (2) the highest k for the later times.
(vii) For small k, the $t = 75$ to 111 evolution is similar to the $t = 72$ to 120 evolution for $\nu = 3.125 \times 10^{-5}$ in figure 7, with the very largest scales (smallest k) still influenced by the original, now decaying, trefoil structure.

https://doi.org/10.1017/jfm.2025.10513 Published online by Cambridge University Press

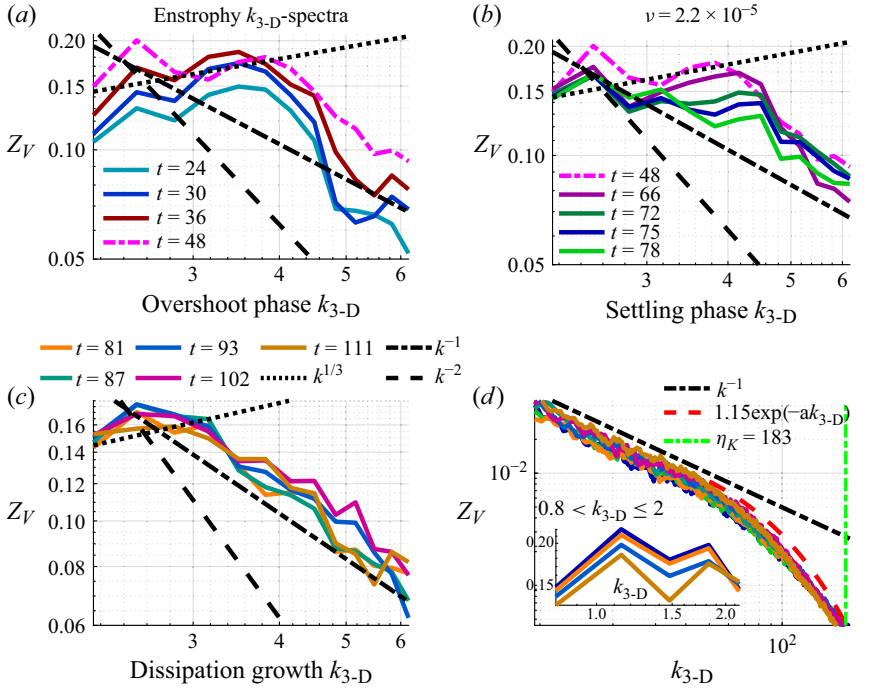


Figure 9. Enstrophy spectra $Z_V(k, t)$ (3.1) for early, intermediate and late times ($t = 24$ to 111) for the highest resolved Reynolds number (Re) calculation ($\nu = 2.2 \times 10^{-5}$) run on a 2048^3 mesh. (*a–c*) Wavenumber span $2 < k < 6$ with $t = 48$ shown in both panels (*a*) and (*b*). For $t \leqslant 36$ in panel (*a*), the spectra briefly overshoot $k^{1/3}$. Panel (*b*) provides the best evidence for persistant, approximately $Z(k, t) \sim k^{1/3}$ for $2.67 \leqslant k \leqslant 4.33$ over a finite time span of $t = 66$ to 75, and less to $t = 78$. Recall that $t \sim 70$ is roughly the time when convergence of the dissipation rates $\epsilon(t)$ begins in figure 6. Note that the leading high-wavenumber of that $k^{1/3}$ span increases slightly with time to $t = 78$. Panels (*c*) and (*d*) show the same times with the $k^{1/3}$ span continuing to retreat for $t > 78$, then decaying for $t > 93$. Panel (*d*) shows both very high and very low wavenumbers. At high wavenumbers, there is a continuation of the $k \geqslant 5$ formation of a k^{-1} enstrophy spectral regime from panel (*c*), with the Kolmogorov-dissipation wavenumber $k_\eta = 183$ noted. The k^{-1} decay persists until $k \sim 50 \sim k_\eta/4$, with approximately exponential decay for $k > 50$, indicated by the rough red-dashed fit. The inset of panel (*d*) shows very low wavenumbers of $k \leqslant 2$ with those $Z_V(k, t)$ decreasing with k, resuming the trend shown in figure 7.

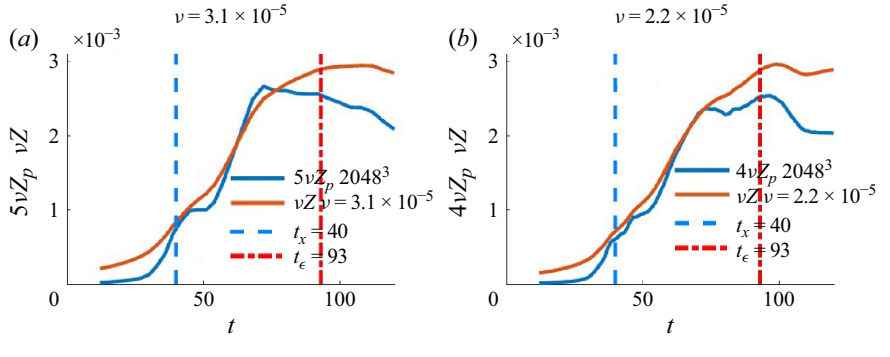


Figure 10. Time evolution of the dissipation rate $\epsilon(t) = \nu Z(t)$ and its scaled production $C_p \nu Z_p(t)$, where $Z_p = \int \zeta_p \, \mathrm{d}V$ and the C_p are chosen to allow comparisons. For these two resolved Reynolds numbers, $Z(t)$ and $C_p \nu Z_p(t)$ follow one another for $t_x \leqslant t \lesssim t_\epsilon$.

https://doi.org/10.1017/jfm.2025.10513 Published online by Cambridge University Press

(viii) For $k > 10$, $Z_V \sim k^{-1}$ from the $k \sim 6$ span continues to dominate for $k \leqslant 50$, followed by approximately exponential k-spectra for $k > 50$. Is this exponential regime consistent with the type of exponential regimes reported for forced turbulence? To determine that requires that a characteristic high, dissipation range wavenumber be defined. Using $\epsilon = \nu Z$, the enstrophy Z is modified within the formula for the effective Kolmogorov wavenumber, $k_\eta = (\epsilon/\nu^3)^{1/4}$, is as follows.

(ix) If turbulence fills the entire domain, using the volume-integrated enstrophy Z (1.13) would be the appropriate choice for determining ϵ and k_η. However, that choice is inappropriate for these calculations because significant vorticity occupies only a fraction of the compuational domain.

(x) Since most of the enstrophy remains within the $t = 0$ inner $(2\pi)^3$ domain, that inner domain has been used to determine k_η, with the relevant volume-averaged enstrophy, dissipation rate and Kolmogorov-dissipation wavenumber being

$$Z_{\Omega 2\pi} \sim Z/(2\pi)^3\,, \quad \epsilon_{\Omega 2\pi} = \nu Z_{\Omega 2\pi} \quad \text{and} \quad k_\eta = (\epsilon_{\Omega 2\pi}/\nu^3)^{0.25}. \tag{3.7}$$

Based upon this, $k_\eta = 183$ and is marked within the exponential regime in figure 9(*d*). Additionally, based on having an exponential wavenumber regime after the power-law regimes, these simulations are resolved.

(xi) Is this k_η-based exponential regime consistent with what has been observed previously for numerical turbulence? For those comparisons, k_ϵ is taken to be where the $Z_V(k, t) \sim k^{1/3}$ regime ends. For both forced turbulence (Kerr 1990; Ishihara *et al.* 2009) and for the algebraic, anti-parallel case (Kerr 2013*b*), $k_\epsilon \sim k_\eta/6$. (Note: k_η was not given for the Gausian profile anti-parallel case (Yao & Hussain 2020).)

(xii) For this case, $k_\epsilon \sim 4{-}5 \approx 0.02 k_\eta$, which is inconsistent with those cases. However, where the $Z_V(k, t) \sim k^{-1}$ regime in figure 9(*d*) ends is at $k \sim k_\eta/6$.

(xiii) Is there another diagnostic that could support how $Z_V(k, t)$ moves to large k in figure 9(*b*)? Two options are the energy transfer spectra (3.4) and the enstrophy production spectra $\zeta(k, t)$ (3.6). The drawback to both is that there are compensating negative and positive values, making it impossible to get useful averages as a pulse moves to large wavenumbers. Introducing time-lags might be applied later (Kerr 1990).

As an alternative, figure 10 follows the global time evolution of the dissipation rate $\epsilon = \nu Z(t)$ and its scaled production $C_p \nu Z_p(t) = C_p \nu \int \zeta_p \, \mathrm{d}V$, ((1.13), (3.6)). Note that $5\nu Z_p(t)$ and $4\nu Z_p(t)$ follow their respective $\epsilon = \nu Z(t)$ for $t_x = 40 \leqslant t \lesssim 70 < t_\epsilon$, suggesting (if dissipation is ignored) that over this period, there is an effective stretching that is maintained within the coiled structures. This would allow for the accelerated, exponential growth of $Z(t)$ and $\epsilon(t)$.

4. Three-dimensional structural evolution

In this section, two phases of the structural evolution of these flows are addressed. One is the $t \leqslant t_x \approx 40$ phase with $\sqrt{\nu} Z(t)$ convergence highlighted in figure 3. The other has the first hints of how the vortices evolve to generate the approximate ν-independent $\epsilon = \nu Z(t)$ convergence in figure 6.

For three-fold symmetric trefoils with algebraic core profiles, the sign of the helicity-density h is taken with respect to the $t = 0$, global (positive) h. Additionally, as before (Kerr 2023), negative-h vortex sheets are shed between the reconnecting vortices, unlike the localised braids and bridges that appear when Gaussian/Lamb–Oseen profiles are used, as reviewed recently (Yao & Hussain 2022) and much earlier (Kida & Takaoka 1994).

https://doi.org/10.1017/jfm.2025.10513 Published online by Cambridge University Press

There are these further differences with the Kerr (2023) trefoils. A different size, a different core circulation and it is perturbed. The size and circulation change the characteristic nonlinear time scale t_{NL} (1.11) and related times such as t_x, accordingly.

The perturbation changes the sequence of reconnection phase events that eventually lead to the production of the finite-time, finite-energy dissipation in figure 6. Figures 11, 12, 13 and 14, for $t = 24$, 30, 42 and 48, show the preliminary steps, but do not continue into the final dissipation phase, which will require another paper. Several isosurfaces and/or views are shown for each of these times.

The major change from the symmetric, algebraic trefoils when it is perturbed is in how the vortical structures evolve at and around the three trefoil crossings, or knots, before self-reconnection begins. To begin, vortex sheets are shed from only two of the knots. These sheets then interact with one another and generate the vorticity maxima around the location of the third knot. It is within this region that the $t > 40 = t_x$ enstrophy growth accelerates as reconnection begins to split it apart.

Figure 11 presents two views of the two vortex sheets that have formed by $t = 24$. The origin of the negative helicity-density, $h < 0$, sheets begins with the positions of the minima (maximum negative values) of the h_f transport term in the helicity budget equation (1.14), which Kerr (2023) studied in detail.

What the local h_f terms do is they push $h>0$ towards local maxima of the helicity-density h and vorticity on the vortex lines, with $h<0$ pushed in the opposite direction as the vortex tubes are flattened due to the coincidence of the local $\min(h_f)$ with local vorticity compression, which are local negative maxima of the enstrophy production term ζ_p in (1.13).

(i) Consider the maroon star at the bottom of figure 11(*a*) with one of the local negative h_f. Here, $h > 0$ is flowing towards the local $\max(h)$, blue hexagon to the right.
(ii) Additionally, $h < 0$ to the left, towards the global $\min(h) < 0$ at the edge of the developing $h < 0$ sheet highlighted in figure 11(*b*).
(iii) Where the global $\min(h_f)$ is located, there is also local $\min(\zeta_p) < 0$ enstrophy compression (1.13), which is pushing that $h < 0$ out into the developing sheet.

These vortex sheets do not appear simultaneously due to the initial perturbation and the panels of figure 11 at $t = 24$ can tell us about the origins of that later progression.

(i) The $t = 24$ details are the following.
(ii) Figure 11(*a*) is a tilted $x-y$ plan view that indicates all three zones of activity while also highlighting the first yellowish $h \leqslant 0$ vortex sheet on the right. This sheet originated from the blue star near the top, the position of ω_m at $t = 21$, with its first growth shown by the orange blob to its right. At $t = 24$, this sheet is sitting between two legs of the original trefoil on the right.
(iii) The focus of figure 11(*b*) is upon the vortex sheet on the left in figure 11(*a*) from a different perspective. This sheet is being actively spawned out of the new positions of ω_m, $\max(h) = h_{mx}$, $\min(h) = h_{mn}$ and $\min(h_f)$, the helicity flux minimum (1.14), whose importance in spawning vortex sheets has been recently discussed (Kerr 2023).
(iv) The third location of strong activity at $t = 24$ is indicated by the maroon $\star$ at the bottom. This location will not generate its own vortex sheet. Instead, starting at $t \sim 30$, this becomes the location around which the two previously generated sheets wrap around one another.
(v) Another role played by the vortex sheets as they extend over time is in how their unseen edges reach the periodic boundaries, which then push back against the

https://doi.org/10.1017/jfm.2025.10513 Published online by Cambridge University Press

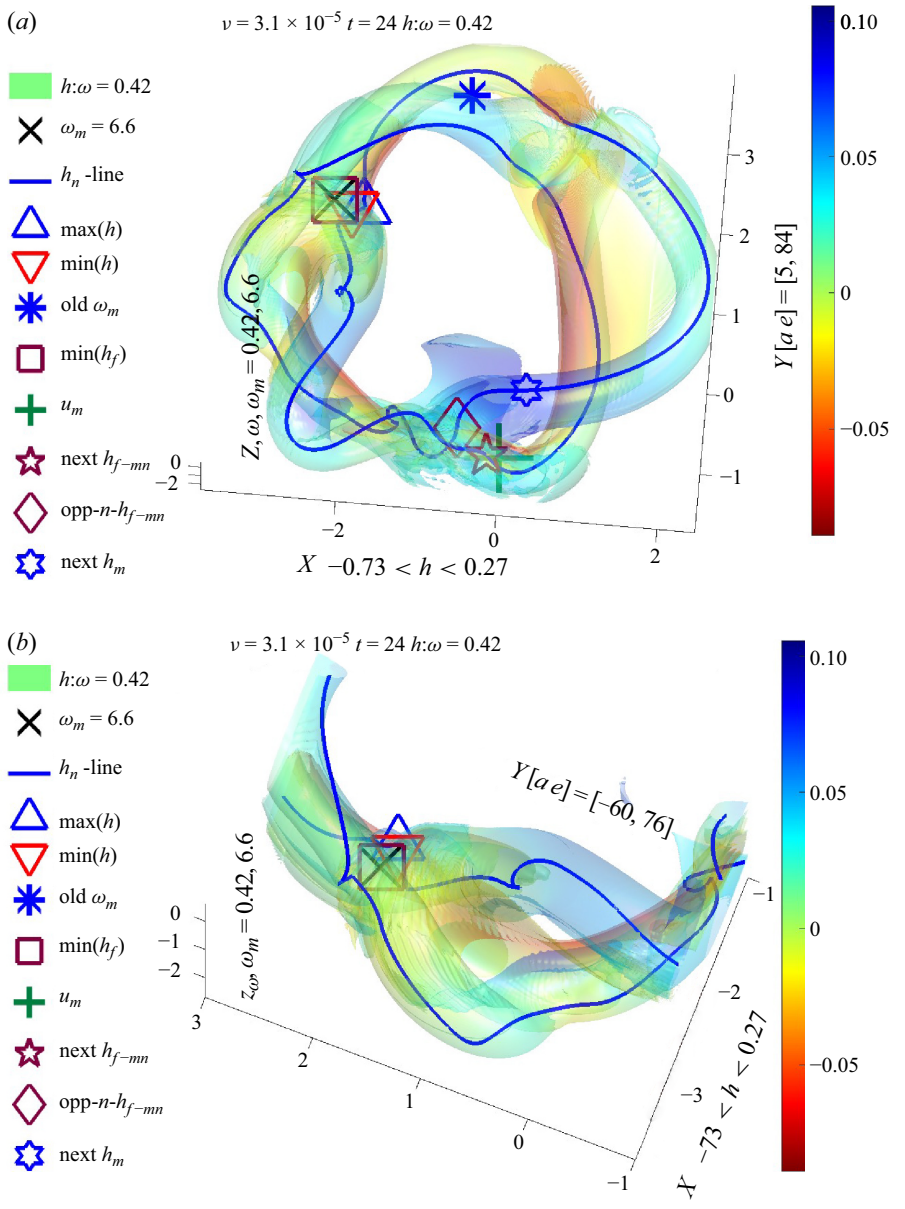


Figure 11. Helicity-mapped vorticity isosurfaces from the 6π-$\nu = 3.125 \times 10^{-5}$ trefoil vortex knot showing the appearance of reddish to yellow negative helicity-density, $h < 0$ vortex sheets. These are being shed off of the blue, predominantly $h > 0$, positive helicity cores of the trefoil vortex, similar to that shown for three-fold symmetric trefoils (Kerr 2023) at $t = 3.6t_{NL}$. Due to the initial perturbation, the evolution of the sheets at the three crossing locations are at different stages of development. (*a*) The yellowish $h \lesssim 0$ sheet on the right begins to form at $t \gtrsim 21$ around the $t = 21$ blue $\star$ at the top. The sheet on the left forms around the current upper-left positions of $\omega_m = \max(\omega) = 6.6$, $h_{mx} = \max(h)$, $h_{mn} = \min(h)$ and $h_{f-mn} = \min(h_f)$. A third sheet might have formed at the bottom, but in this asymmetric case, what happens instead is that the pre-existing sheets wrap around one another, as shown in the next two figures. (*b*) Focus on left zone vortex sheets around the positions of ω_m, $\max(h)$ and $\min(h)$, rotated such that the sheets are exposed. The strongest $h < 0$ is coming off the outer (bottom) trefoil leg, with a yellow $h \lesssim 0$ vortex sheet between the two legs of the trefoil.

https://doi.org/10.1017/jfm.2025.10513 Published online by Cambridge University Press

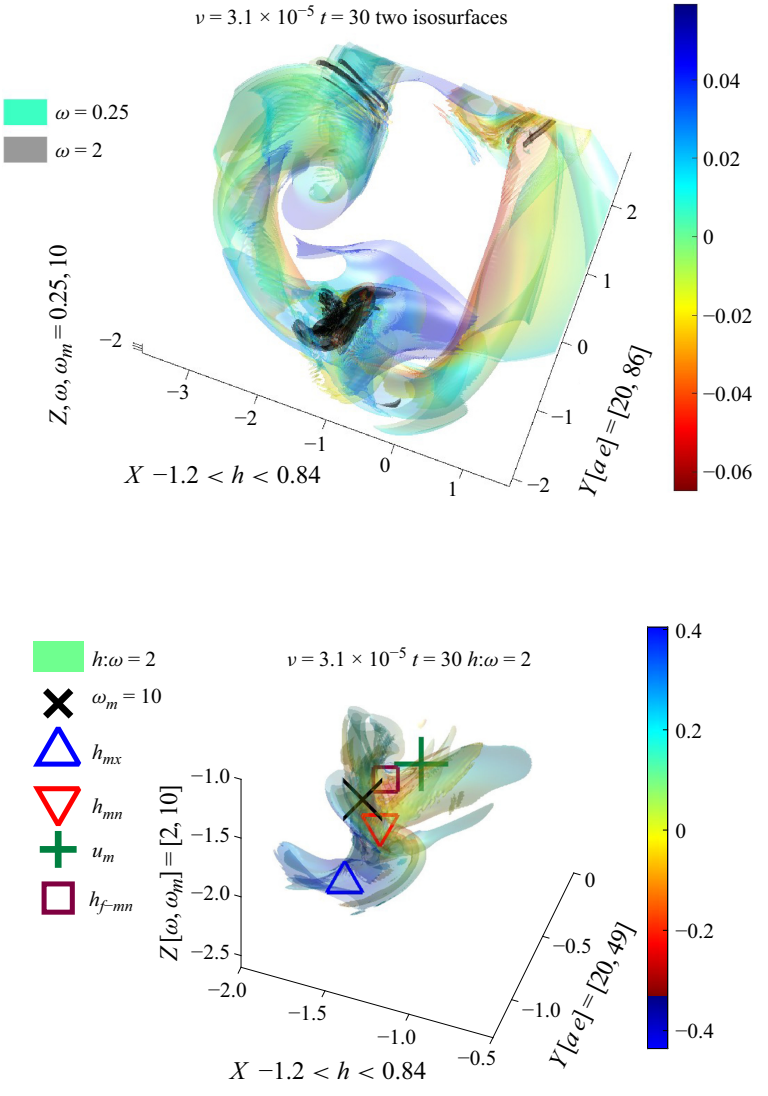


Figure 12. Vorticity isosurfaces at $t = 30$. This and the following two figures focus on the zone at the bottom from $t = 24$, with the vortex sheets from figure 11 now winding around one another. In both frames, $\omega = 2$ vorticity isosurfaces are shown with the maximum vorticity having increased from $\omega_m = 6.6$ at $t = 24$ to $\omega_m = 10$ at $t = 30$. (*a*) Relationship between the primary $\omega = 2$ isosurface in black and the helicity-mapped $\omega = 0.25$ isosurfaces that show the rest of the trefoil. (*b*) A $\omega = 2$ helicity-mapped isosurface to indicate the active wrapping of the previously ($t = 24$) formed isosurfaces, which leads to the formation of an intense localised vortex knot.

growing sheets. This effect can provide us with an empirical explanation for the origin of the observed critical domain size parameter $\ell_c \sim \nu^{-1/4}$ (2.1). Another example of the expanding sheets is given by figure 22 of Kerr (2023).

Reconnection phase figures 12 and 13 at $t = 30$ and 42 show the further development around that bottom location. Both $t = 30$ frames in figure 12 include $\omega = 2$ isosurfaces. Figure 12(*a*) is dominated by a temporally extended, smaller vorticity, $\omega = 0.25$, isosurface that is a version of the $t = 24$ helicity-mapped vortex sheets from figure 11(*a*) and is

https://doi.org/10.1017/jfm.2025.10513 Published online by Cambridge University Press

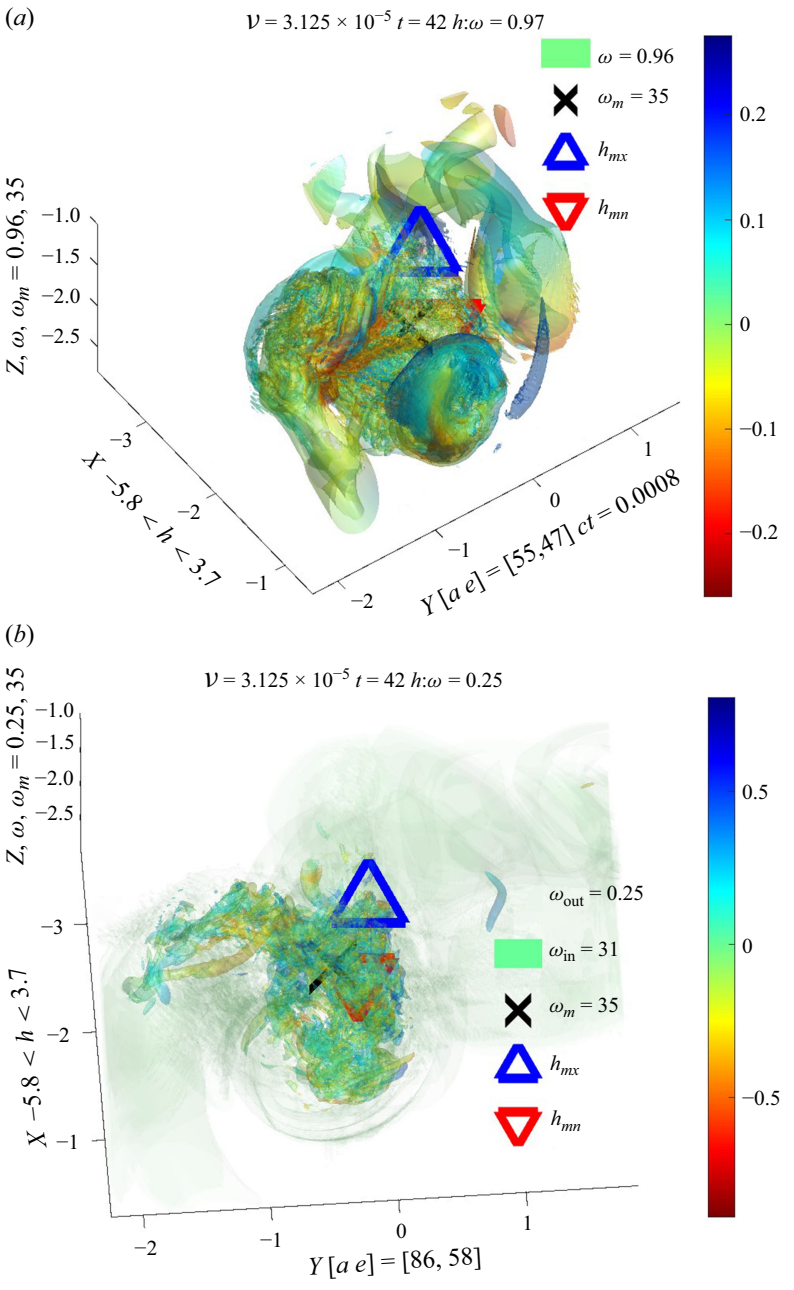


Figure 13. (*a*) Wrapping of $\omega = 0.96$ isosurfaces around an inner core similar to that for $t = 30$ in figure 12(*b*). Within the more tightly wound structure around $y \sim 0$, the maximum vorticity has increased from $\omega_m = 10$ at $t = 30$ to $\omega_m = 35$ at $t = 42$, indicated by the barely visible vorticity and helicity-density extrema, ω_m, h_{max} and h_{min}. This wrapping is a prelude to the accelerated enstrophy production for $t > t_x \sim 40$. A new feature is a series of vortex tubes on the left that have aligned with one another. (*b*) Two additional isosurfaces. The smaller $\omega = 0.25$, $h \sim 0$ greenish isosurface shows how this knot is connected to the rest of trefoil and the $\omega = 31$ isosurface shows early-stage tangled vortex structures forming within the two legs, with that on the left more obvious than that around h_{min} (red).

https://doi.org/10.1017/jfm.2025.10513 Published online by Cambridge University Press

overlaid with several higher vorticity grey (single colour) isosurfaces. Two small, remnant grey surfaces at the top of figure 12(*a*) show where the knots that created the two $t \leqslant 24$ surfaces were, with a major convoluted surface at the bottom of figure 12(*a*) being where those two $t = 24$ isosurfaces are now interacting.

Figure 12(*b*) maps the helicity-density onto that higher vorticity isosurface at the bottom, generating a structure that shows how two vortex sheets from $t = 24$ are becoming a single structure consisting of the paired vortex sheets, which are being pulled together, then starting to wrap around one another. All the primary vorticity and helicity-related extrema are within this structure.

Figure 13 at $t = 42$ shows what is left as the outer vortex sheets from $t = 30$ begin to dissipate, leaving behind a $\omega = 0.96$ local jellyroll of vortex sheets in figure 13(*a*) that seems to be breaking apart.

Figure 13(*b*) has two isosurfaces. The green $\omega_{out} = 0.25$ isosurface shows how this region is still connected to the rest of the trefoil in figure 12(*a*) and a high threshold, helicity-mapped $\omega_{in} = 31$ isosurface showing a transition within the $\omega = 0.96$ jellyroll in figure 13(*a*). One that is transforming the vortex sheet wrapping of the jellyroll into coiled and tangled structures, which is the type of configuration that would be capable of generating the strong increases in the enstrophy that are required for eventually yielding the large, finite energy dissipation rates in figure 6.

Figure 14(*a*) at $t = 48$ shows an outer $\omega = 0.73$ isosurface of the jellyroll noted at $t = 42$ whose transformation can now be described as a splitting, with the inner $\omega = 2.1$ isosurfaces in figure 14(*b*) showing how the evolution of the tangles at $t = 42$ in figure 13(*b*) are at $t = 48$, developing into separate spiralling vortices within the two halves of the split knot.

Note that this $t > t_x \sim 40$ spiralling develops when the enstrophy growth accelerates strongly enough to generate the convergent dissipation rates in figure 6, and also when the scaled enstrophy production rates $C_p \nu Z_p(t)$ (3.6) follow the dissipation $\epsilon(t)$ and enstrophy $Z(t)$ growth in figure 10. This suggests that the growth is exponential, with the required stretching that was missing from the original model (Lundgren 1982) being internally generated by the spirals. This accelerated growth would also be the source of the transient span of mid-wavenumber Kolmogorov scaling $Z_V(k) \sim k^{1/3}$ regimes in figure 9(*b*). Showing how this wrapping, or an equivalent small-scale dynamics, continues to later times will be the topic of another paper.

5. Summary of using large $(2\ell\pi)^3$ domains

This paper has focused on two aspects of the large domain, higher Reynolds number trefoil calculations that were not fully covered by the earlier trefoil calculations of Kerr (2018*b*, 2023).

The first aspect, in §§ 2.1–4, extends the numerical analysis of the perturbed trefoil calculations from before (Kerr 2018*b*), by covering later times with higher resolution for many. Plus one new calculation.

These extensions begin with enlargements of the computational domains at mid- to late-times so as to maintain the observed temporal convergence of $\sqrt{\nu} Z(t)$ at $t = t_x \approx 40$ in figure 2, and then approximate convergence of the dissipation rate $\epsilon = \nu Z$ for $t \sim t_\epsilon = 93 \sim 2t_x$ in figure 6. This enlargement included the smallest viscosities/highest Reynolds numbers calculations, all of which are indicated by dash-dotted lines and are somewhat under-resolved, These are $\nu = 1.56 \times 10^{-5}$, 7.8×10^{-6} and 4×10^{-6}.

Previously, $t_x \approx 40$ was identified from vortex structures as the end of the reconnection phase (Kerr 2018*a*), and then as the transition from the inverse-linear $(\sqrt{\nu} Z(t))^{-1/2}$

https://doi.org/10.1017/jfm.2025.10513 Published online by Cambridge University Press

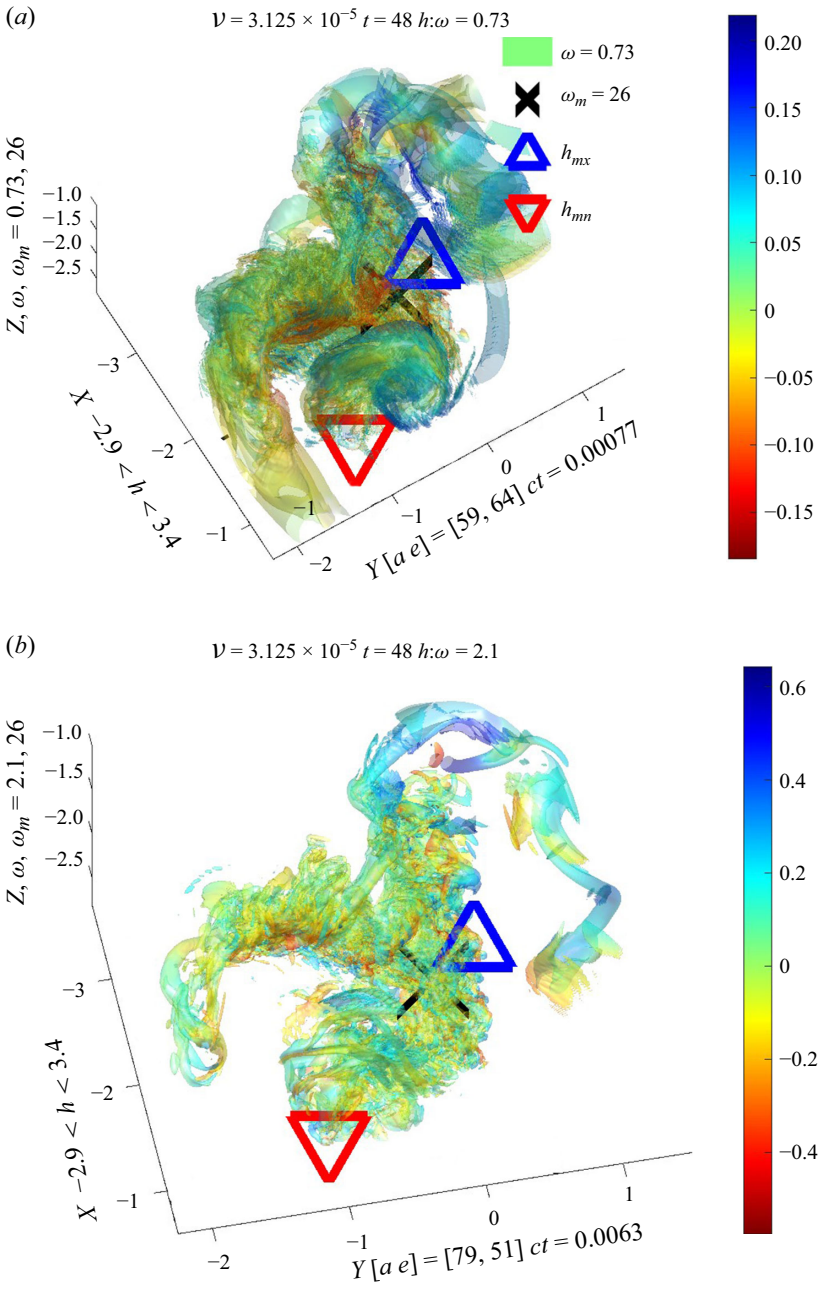


Figure 14. (*a*) A $\omega = 0.73$ isosurface similar to that from $t = 42$, except there is a clearer separation between the left side and wound-up right side. The $\omega = 2.1$ isosurface in panel (*b*) makes this post-$t = 42$ split more obvious. In addition, the spirals of its higher vorticity, and smaller scale, isosurfaces are more organised as they wrap around their respective centrelines. The continuing evolution of these spiralling sheets would be consistent with the accelerated growth in the enstrophy that leads to the finite dissipation ΔE_ϵ shown in figure 6. This is distinctly different than the vortex braids winding around reconnected trefoils seen when Gaussian profiles are used and yield suppressed dissipation rates (Yao *et al.* 2021; Kerr 2023).

https://doi.org/10.1017/jfm.2025.10513 Published online by Cambridge University Press

behaviour (Kerr 2018*b*), as in figure 3. What follows next is the accelerated enstrophy growth that leads to convergence of the energy dissipation rates $\epsilon = \nu Z(t)$ in figure 6. That $t_x \approx 40$ is the time when physical space reconnection begins is shown here using graphics at $t = 42$ and 48 in figures 13 and 14.

Figure 6 shows that the convergence of $\epsilon(t)$ begins at $t \sim 70$ and persists for approximately $\Delta T \sim t_x$. When the $\epsilon(t)$ are temporally integrated, this is long enough to yield approximately ν-invariant finite ΔE_ϵ (1.2), satisfying one definition for a dissipation anomaly. This $\epsilon(t) = \nu Z = \nu \mathcal{O}_{V1}^2$ convergence can be obtained over the full factor of 125 decrease in ν and is consistent with these being turbulent flows. However, convergence of the higher-order $m > 1$ $\mathcal{O}_{Vm}(t)$ moments at these later times can only be achieved over a factor of 25 in the Reynolds number. Figure 9 shows that for these mid-range Reynolds numbers, the mid-wavenumber spectral slopes with $Z_V(k, t) \sim k^{1/3}$ are Lundgren-like, providing further evidence for the appearance of classical turbulence.

5.1. *Supporting numerical analysis and mathematical scaling for* $(2\ell\pi)^3$ *domains*

The second aspect is providing new quantitative numerical analysis and mathematical scaling to explain why the computational domains need to be increased. Because they are compact, trefoil vortex knots have been ideal for showing that the $B_\nu(t)$ (1.15) scaling can be retained as ν decreases by increasing the domain size, leading to the following question. What controls the domain dependence of the enstrophy suppressing critical viscosities?

Previously, to maintain the temporal convergence at t_x, the domain size $\mathcal{L} = 2\ell\pi$ had to be empirically increased as ν decreased (Kerr 2018*a*,*b*), although an estimate of that dependence was not given. Here, with a wider range of ν, especially for the convergence of $(\nu^{1/4}\Omega_\infty)^{-1}$ at $t_\infty \approx 18.4$, combined with the consistency of the convergence of each $(t < t_x)$ $(\nu^{1/4}\mathcal{O}_{Vm}(t))^{-1}$, it is clear that the increase is $\ell \sim \nu^{-1/4}$. The structural evidence points to the growth of vortex sheets as in figures 11 and 12(*a*) as the source of the limiting factor. Overall, combining the requirements at large scales with $\ell \sim \nu^{-1/4}$, with those at small scales going as $\eta \sim \nu^{3/4}$, the range of scales should increase as $\ell/\eta \sim \nu^{-1/4}/\nu^{3/4} \sim \nu^{-1}$.

A more rigorous supporting result is given in Appendix A. This provides an extremal mathematical justification for why increasing ℓ is needed. The method consists of determining domain size dependent mathematical critical viscosities $\nu_s(\ell)$ as ℓ increases. These analytic/Sobolev $\nu_s(\ell)$ are found by rescaling the high-order $s > 5/2$ Sobolev analysis for $\ell = 1$, $V = (2\pi)^3$ into larger $V_\ell = (2\ell\pi)^3$ domains (1.16). With some $(2\pi)^3$ estimates of the ν_s made from the Euler norms in Appendix A.5, before they are transformed into the original domain in Appendix A.6.

Is there mathematics that could bring the two determinations of the critical viscosities more in line with one another? Currently, we know that the $\nu_s(\ell)$ should be, and are, orders of magnitude smaller than the empirical ν_c. However, it is believed by many that $\ell \to \infty$ limiting behaviour can be determined by a more direct extension of the $(2\pi)^3$ mathematics (Constantin 1986) to whole space, infinite $\mathbb{R}^3$. Part of that extension has been done (Robinson 2021) and having a further extension might bridge that gap by showing explicitly how the $\nu_s(\ell)$ depend upon ℓ, the domain size.

The conclusion of both approaches is that getting a dissipation anomaly that is finite-time finite-ΔE_ϵ, without finite-time singularities, is possible only when the physical problem is done in whole space, that is, infinite $\mathbb{R}^3$.

5.2. *Spectral summary*

In addition to generating convergence of $\epsilon(t) = \nu Z(t)$, then finite dissipation ΔE_ϵ (1.2) during the period $t \gtrsim 72$, precursors to $k^{1/3}$ spectral scaling also develop, from short

https://doi.org/10.1017/jfm.2025.10513 Published online by Cambridge University Press

$Z_V(k) \sim k^{1/3}$ regimes for $3 \leqslant k \leqslant 4$ at $t = 72$ and 80 for $\nu = 3.12 \times 10^{-5}$ to slightly broader $2.67 \leqslant k \leqslant 4.33$ regimes for $t = 66$ to 78 for $\nu = 2.2 \times 10^{-5}$. These are distinctly less steep than the $E(k) \sim k^{-7/3}$ spectra, or equivalent $Z(k) \sim k^{-1/3}$, reported for a Gaussian-profile trefoil (Yao *et al.* 2021), whose decrease in energy is approximately 25 % over that span. By integrating $\epsilon(t)$ from figure 6, the algebraic trefoil's energy decays by approxomately 50 % as the coiled vortices shown in figures 13 and 14 form.

(i) These indications of enstrophy and energy flow through wavenumbers are usually associated with turbulent flows, showing that for these and the earlier Kerr (2023) calculations, an energy cascade to small scales does not require the formation of a statistically steady state and instead can form as the enstrophy moves through a brief $Z_V(k) \sim k^{1/3}$ regime, as in figure 9(*b*).

(ii) However, are these transient quasi-$k^{1/3}$ regimes consistent with the experimental observations of Kolmogorov spectra from statistically steady data? They are not, as shown by how the $Z_V(k) \sim k^{-1}$ spectrum persists after the convergence of the dissipation rates after $t_\epsilon \sim 93$. Specifically ,to $t = 120$ for $\nu = 3.12 \times 10^{-5}$ in figure 7 and $t = 111$ for $\nu = 2.21$ in figure 9(*d*), along with how the Kolmogorov wavenumber (3.7) is unexpectedly large.

(iii) Perhaps this should be expected, because unlike these calculations, having a statistically steady state implies the existence of a steady energy source, such as a constant flow, forcing or in the algebraic anti-parallel case (Kerr 2013*b*), very long initial vortices, which allows for the formation of multiple reconnection sites with coiled or twisted vortices. Additionally, with multiple reconnection sites, off-set in time, it is likely that the contributions to the spectra from these sites overlap, allowing for smoother-in-k evolution of the spectra.

5.3. *Does* $(2\ell\pi)^3$ *rescaling lead to turbulence?*

Is this evidence for a dissipation anomaly and Lundgren-like spectra consistent with the seminal proposal of Onsager (1949) that there might be singularities, or near singularities, around which spatial velocity increments have a 1/3 Hölder exponent (Eyink 2003), from which $k^{-5/3}$ Kolmogorov spectra and finite dissipation might develop.

In a strict sense, the existing numerics does not support a role for singularities. Singularities of either the Navier–Stokes or Euler equations away from boundaries have not been identified, with the strongest growth for the Euler equations being doubly exponential (Kerr 2013*a*; Meng & Yang 2024). The latest forced, very-high-Reynolds-numbers calculations are not providing convincing numerical evidence because the dissipation rate ϵ (1.12) increases slowly when the Reynolds numbers are increased (Iyer, Sreenivasan & Yeung 2022). Given these difficulties, a possible role for sub-Kolmogorov fluctuations has been floated (Eyink & Jafari 2022).

However, if one replaces the assumption of singularities with how vortex sheets are shed, the calculations here present an alternative approach to generating numerical turbulence with finite dissipation where we have the following.

(i) The large-scale forcing is replaced by large-scales that grow without bounds.

(ii) The first vorticity that is shed from the original configuration is in sheets, not thin bridges or braids, with the finite-time energy dissipation resulting from the interactions between those sheets.

(iii) When there is only one self-interaction and reconnection site, and the energy flow through the wavenumbers is not continuous, but occurs as a pulse. A pulse whose

https://doi.org/10.1017/jfm.2025.10513 Published online by Cambridge University Press

slope is consistent with 1/3 scaling as the time convergent dissipation rates are reached.

These observations demonstrate that the incompressible Navier–Stokes are capable of generating many, but not all, of the properties of fully developed Navier–Stokes turbulence, without the types of Navier–Stokes modifications referenced previously.

6. Summary

Taken together, it has been shown that by increasing the domains for these unforced calculations, finite-time dissipation can be achieved over a wider range of viscosities ν and Reynolds numbers Re than those reported by Kerr (2023). For the shed vortex sheets, having large domains places fewer constraints upon their growth before they begin to wrap around one another. Also presented is evidence for precursors to Kolmogorov- or Lundgren-like scaling. To close this paper, a number of questions are now presented, some of which are currently being addressed.

Is convergent scaling by $\sqrt{\nu}Z(t) = \left(\nu^{1/4}\mathcal{O}_{V1}(t)\right)^2$ unique to trefoils? In published calculations, the equivalent $B_\nu(t) = (\nu^{1/4}\mathcal{O}_{V1})^{-1}$ scaling (1.15) has been identified for trefoils with different core thicknesses (Kerr 2018*a*), symmetric trefoils in a $(2\pi)^3$ periodic box (Kerr 2023) and nested coiled rings (Kerr 2018*c*). In ongoing work, $\mathcal{O}_{Vm}(t)$ scaling (1.1) is being applied to the Taylor–Green vortex (Brachet *et al.* 1983) and new versions of recent orthogonal vortices calculations (Ostillo-Monico *et al.* 2021).

What is the origin of the $\nu^{1/4}$ scaling? Lengths with a $\sqrt{\nu t}$ dependence are common in fluid theory. One example is how the compression perpendicular to the stretching along the Burgers vortex is balanced by the perpendicular viscous terms. Another example is how some of the most refined mathematics uses Leray (1934) scaling with $\delta_\nu(t) \sim \sqrt{2\nu(T-t)}$ to restrict singularities of the Navier–Stokes equations (Necas, Ruzicka & Sverák 1996; Escauriaza, Seregin & Sverák 2003). However, Leray scaling is about collapsing to a point, not to the type of sheets observed here.

Could these vortex sheets be the source of the $\nu^{1/4}$ scaling? An answer should come from how the sheets form out of the helical knots within the trefoil configurations, here and as reported by Kerr (2023), which are themselves strongly helical. These knots exist where the loops of the trefoil cross and tend to block the evolution of the trefoil.

The flows resolve that constraint by generating negative helicity, $h < 0$, vortex sheets like those in figures 11 and 12, thereby circumventing the helical knots. This formation of $h < 0$ vortex sheets is balanced by simultaneous increases of $h > 0$ on the trefoil's cores, as at the bottom of figure 11(*a*) and more explicitly reported by Kerr (2023), resulting in increases in the vorticity, and enstrophy, along those cores without violating the pre-reconnection, nearly Euler, conservation of the global helicity.

To go further requires examining the details of interactions like that shown in figure 12(*b*), where a pair of vortex sheets are interacting. The detailed centreline vorticity analysis of vortex stretching and compression reported by Kerr (2023), along with new analysis of similar interactions for initially orthogonal vortices, show the following. Between the pair, there is compression pushing the vortices together. When that is balanced by viscous diffusion, a length might form that goes as $\delta(\nu) \sim \sqrt{\nu}$. This compression could then be balanced by expansion and stretching in the two perpendicular directions that goes as $\nu^{-1/4}$, a process best seen in figure 12(*b*).

Does the influence of $\nu^{1/4}$ scaling and formation of double vortex sheets extend further in time? It does in the sense that double vortex sheets are required for the post-reconnection

https://doi.org/10.1017/jfm.2025.10513 Published online by Cambridge University Press

enstrophy growth to accelerate sufficiently to get finite-time energy dissipation, ΔE_ϵ (1.2), and is consistent with how the wrapped structure in figure 12(*b*) at $t = 30$ has formed from the two vortex sheets at $t = 24$ in figure 11. The spiral vortex model of Lundgren (1982) assumed only a single vortex sheet spiralling around a central vortex, which is distinctly different than the paired sheets of both this trefoil and orthogonal vortices.

To accomplish any of these further objectives, new calculations will be required. We could start with extending the Reynolds number range of the $m > 1$ $\Omega_m(t)$ convergence in figure 5 to the $\nu = 1.56 \times 10^{-5}$ and $\nu = 7.8 \times 10^{-6}$ cases, which should be re-run in $(8\pi)^3$ domains on 4096^3, or equivalent, meshes. This should provide for both adequate resolution on the small scales and sufficient padding at the largest scales to control interactions with the periodic boundaries.

Acknowledgements. I would like to thank the Isaac Newton Institute for Mathematical Sciences for support and hospitality during the programme *Mathematical Aspects of Fluid Turbulence: where do we stand*? in 2022, when work on this paper was undertaken and supported by grant number EP/R014604/1. Further thanks to E. Titi (Cambridge) who suggested using domain rescaling and J.C. Robinson (Warwick) who shared his version of the earlier nonlinear inequality (Constantin 1986). Computing resources have been provided by the Scientific Computing Research Technology Platform at the University of Warwick.

Declaration of interests. The authors report no conflict of interest.

Appendix A. Domain rescaling

Can the empirical evidence for dependence of $\nu_c(\ell)$ (2.1) be understood analytically? The Appendix shows how related analytic critical viscosities ν_s, originally estimated using $(2\pi)^3$ analysis (Constantin 1986), decrease as ℓ increases through rescaling of that analysis to larger $(2\ell\pi)^3$, $\ell > 1$, domains. This in turn allows the formation of dissipation anomalies as ℓ increases.

In the past, it has been claimed that this can be done by supposing extensions into whole space, infinite $\mathbb{R}^3$, using the 'usual methods'. One version of that approach is to create new outer, whole space length scales out of ratios of higher-order Sobolev norms. An approach that requires additional estimates that might also depend upon the viscosity.

The approach here is incremental, showing how the $\nu_s(\ell)$ (A31) critical viscosities change as the domain parameter ℓ and domain V_ℓ (1.16) increases, which allows the growth of higher-Reynolds-number solutions without restrictions from $\nu \equiv 0$ Euler solutions (A38). This approach is numerically inspired and upon iteration might be extended to $\mathbb{R}^3$, and makes minimal use of the mathematics for periodic domains. This is in contrast to the complementary result of Robinson (2021) that uses $\mathbb{R}^3$ mathematics, with two primary results. Abbreviated, the result more directly related to this Appendix showed that for a compactly supported velocity (of a vorticity field) with a fixed, sufficiently smooth initial condition $u_\ell(t = 0) \in H^1_\ell(V_\ell)$ (1.21), an appropriate extension of $u_\ell(t)$ converges to a solution of u in $\mathbb{R}^3$. Some of the methods are discussed further by Robinson *et al.* (2016). Part of the reason for the incremental approach is it might be more closely linked to the empirical $\nu_c(\ell)$ result (2.1). One place of overlap with this Appendix is in how (A11) plays an important part in the proof of Theorem 6.2 of Robinson (2021).

Appendices A.2–A.6 show how one can apply scale invariance to avoid introducing new length scales when extending that analysis to larger $V_\ell = (2\ell\pi)^3$ domains. First, one rescales the V_ℓ inner products and norms into a $(2\pi)^3$ domain; then one can calculate the critical viscosities $\nu_{s_{2\pi}}$ as before; and finish by converting the $\nu_{s_{2\pi}}$ into ν_s in the original V_ℓ domain. The primary tools for this analysis are the $\dot{H}^s_\ell = \|u_\ell\|^2_{\dot{s}}$ norms (1.22) defined in § 1.2.

https://doi.org/10.1017/jfm.2025.10513 Published online by Cambridge University Press

Before the rescalings are given, Appendix A.1 presents the domain-dependent rescaling of the variables, properties and norms that will be used throughout. The first rescaling step in Appendix A.2 then applies those rescalings to squeezing the $\|u_\ell\|_{\dot{s}+1}$ Navier–Stokes solutions in large $V_\ell = (2\ell\pi)^3$ domains into a $(2\pi)^3$ domain, followed by application of the resulting $\|u_\lambda\|_{\dot{s}+1}$ $(\lambda = \ell)$ to approximations of the $H^s_{2\pi}$ Sobolev mathematics developed for $(2\pi)^3$ domains.

Next, Appendix A.3 determines difference inequalities for the $w = v - u$ (1.6), with Appendix A.4 providing an alternative way to solve the cubic nonlinearity in those inequalities with integrating factors. This is followed by the determination of the critical viscosities $\nu_{s_{2\pi}}$ in Appendix A.5 using the $H^{s_{2\pi}}$ norms. The sequence of steps in Appendices A.3–A.5 largely follows Chapter 9 of Robinson *et al.* (2016) (with Lemma 1 of the robustness proof being a version of the solution to their problem (9.2)) and is analogous to what was previously found for a $(2\pi)^3$ domain (Constantin 1986).

Finally, those $\nu_{s_{2\pi}}$ are rescaled back to the original $(2\ell\pi)^3$ domain in Appendix A.6, resulting in decreasing $\nu_s \sim \exp(-\int_0^t \lambda^{s+1}\|u_\ell(\tau)\|_{\dot{s}+1}\,\mathrm{d}\tau)\lambda^3$ as $\lambda = \ell$ increases, with the $\|u_\ell(\tau)\|_{\dot{s}+1}$ coming from the original domain and the exponential factor dominating over the algebraic λ^3 factor.

This result can explain why the small ν trefoil results with convergent $\sqrt{\nu}Z(t)$, and then convergent $\epsilon = \nu Z(t)$, are allowed by the mathematics. If extended further by taking $\ell \to \infty$, one might be able identify limiting behaviour in $\mathbb{R}^3$, known as whole space.

A.1. *Rescaling of variables and norms*

For a periodic domain of size $V_\ell = (2\ell\pi)^3 = L^3$, $L = 2\pi\ell$, a rescaling parameter $\lambda = \ell$ is defined that rescales these variables into a $L_0 = 2\pi$, $L_0^3 = (2\pi)^3$ domain:

$$L_\lambda = L/\lambda = 2\pi, \quad U_\lambda = U/\lambda, \quad u_\lambda = u/\lambda \quad \text{and} \quad \nu_\lambda = \nu/\lambda^2, \tag{A1}$$

such that the Reynolds numbers and inverse time/vorticity scales invariant under λ:

$$Re_\lambda = U_\lambda L_\lambda/\nu_\lambda = Re\,, \quad \omega_\lambda = \boldsymbol{\nabla}_\lambda \times u_\lambda = (\lambda/\lambda)\omega = \omega. \tag{A2}$$

The inverse lengths and derivatives when mapped into an L_λ domain are multiplied by λ (left), with their effect upon u (right) as follows:

$$\partial_\lambda = \lambda\partial\,, \quad \boldsymbol{\nabla}_\lambda = \lambda\boldsymbol{\nabla}, \qquad \nabla^s u \to \nabla^s_\lambda u_\lambda = \lambda^{s-1}\nabla^s u = \lambda^{s-1}u_{,s}, \tag{A3}$$

such that for $\|u\|_{\dot{s}}$ in the V_ℓ domain (left), in the V_1 (right) domain, one gets

$$\|u_{,s}\|_0 = \|u\|_{\dot{s}} = \left(\int_{\mathcal{V}_\ell} (\nabla^s u)^2\,\mathrm{d}^3x\right)^{1/2} \Rightarrow \|u_\lambda\|_{\dot{s}} = \left(\int_{\mathcal{V}_1} \lambda^{2s-2}(\nabla^s u_\lambda)^2\,\mathrm{d}^3x\right)^{1/2} = \lambda^{s-1}\|u\|_{\dot{s}}. \tag{A4}$$

A.2. *Squeezing, then rescaling, H^s norms*

Now, extend this scaling to vorticity-related properties and Sobolev norms.

(i) For the circulation:

$$\Gamma_\lambda \sim U_\lambda L_\lambda = \Gamma/\lambda^2 \quad \text{and} \quad a_\lambda = a/\lambda. \tag{A5}$$

(ii) The nonlinear time scale is invariant:

$$T_{NL} = T_\lambda = a_\lambda^2/\Gamma_\lambda = (a^2/\lambda^2)/(\Gamma/\lambda^2) = T_{NL}. \tag{A6}$$

https://doi.org/10.1017/jfm.2025.10513 Published online by Cambridge University Press

(iii) The volume-integrated enstrophy $Z = V\|u\|_1^2 \sim \Gamma^2/L$ such that

$$Z_\lambda \sim (\Gamma^2/L) = Z/\lambda^3. \tag{A7}$$

(iv) The volume-integrated energy $E = (1/2)V\|u\|_0^2 \sim \Gamma^2 L$ so that

$$E_\lambda \sim \Gamma_2 L/(\lambda^2\lambda^2\lambda) = E/\lambda^5. \tag{A8}$$

(v) Finally, the viscous time scale is unchanged:

$$t_\nu = \nu_\lambda \Delta_\lambda u/u \sim \nu/\lambda^2(\lambda^2\Delta u/\lambda)/(u/\lambda) \sim \nu\Delta u. \tag{A9}$$

Classical result. Does this rescaling affect the Hölder and Cauchy–Schwarz inequalities that lead to this classic time inequality? (see Doering 2009 and Theorem 6.2 of Robinson 2020)

$$\frac{\mathrm{d}}{\mathrm{d}t}\|\nabla u\|_0^2 \leqslant \frac{c'}{\nu^3}\|\nabla u\|_0^6. \tag{A10}$$

Here, c' is constant and is independent of the periodic domain size. From this, one gets for $u_0 = u(0)$,

$$\|\nabla u(\cdot, t)\|_0^2 \leqslant \frac{\|\nabla u_0\|^2}{\sqrt{1 - 2c'\|\nabla u_0\|^4 t/\nu^3}}. \tag{A11}$$

Using the denominator of this inequality, the times over which the solutions are ensured to be smooth and unique are

$$0 < t < t_b = \frac{\nu^3}{2c'\|\nabla u_0\|^4}. \tag{A12}$$

Because the rescaled viscosity is $\nu_\lambda^3 = \nu/\lambda^6$ and enstrophy squared is $Z_\lambda^2 = \|\nabla u\|^4 \sim Z/\lambda^6$, after rescaling $t_{b\lambda} = t_b$, such that this time scale (A9) is not affected by the rescaling with λ.

A.3. *Difference inequalities for w with Euler u*

For $\ell = 1$, by using higher-s-order Sobolev time nonlinear inequalities, one can find the $(2\pi)^3$ domain, analytic critical viscosities ν_s that mark the threshold for when $\nu \to 0$ Navier–Stokes solutions can be bounded by $\nu \equiv 0$ Euler solutions. Higher-s-order Sobolev time nonlinear inequalities are used because they allow us to go beyond what the $s = 0$ $(\mathrm{d}/\mathrm{d}t)(1/2)\|u\|_0^2$ equation (1.20) can tell us.

The relevant Sobolev time inequalities are higher-order versions of the s-order inner products between the velocity difference $\boldsymbol{w} = \boldsymbol{v} - \boldsymbol{u}$, higher-order time derivatives $\nabla^s w_t$ and its equation (1.6),

$$\frac{1}{2}\frac{\mathrm{d}}{\mathrm{d}t}\|w\|_s^2 + \nu\|w\|_{s+1}^2 \leqslant \nu\|u\|_{s+1}\|w\|_{s+1} + d_s\|w\|_s^3 + d_s\|u\|_s\|w\|_s^2 + c_s\|u\|_{s+1}\|w\|_s^2. \tag{A13}$$

The resulting inequality equations have several cubic nonlinearities and two sets of constants. For order s terms, c_s, and for nonlinear order $s+1$ terms, d_s,

$$c_s = 2^s C_s \quad \text{and} \quad d_s = s2^s C_{s-1} \quad \text{with} \quad C_s \sim L^{-3/2+s}. \tag{A14}$$

The goal is to reduce (A13) to an inequality with a single cubic nonlinearity, then solve it to show if there are bounds upon Navier–Stokes solutions. With a different exposition, the

https://doi.org/10.1017/jfm.2025.10513 Published online by Cambridge University Press

second constant d_s would be unnecessary, but is retained because a different power of L is needed for the parametrisations in (A17).

To get (A13), gradients need to be added to the $B_{NL}(\cdot,\cdot)$ inner products in the w equation (1.6). These become order-s inner products $\langle uv\rangle_s^2$ (1.18), from which w-based energy inequalities can be created. For example,

$$\|B_{NL}(u,w)\|_{\dot{s}} \leqslant c_s\|u\|_{\dot{s}}\|w\|_{\dot{s}+1}. \tag{A15}$$

To find the analytic ν_s, some reductions are needed. The next step is make estimates of the higher-s, inner products of higher-order versions of the three $B_{NL}(\cdot,\cdot)$ nonlinear terms of the $\boldsymbol{w}$ equation (1.6): $(\boldsymbol{u}\cdot\nabla)\boldsymbol{w}$, $(\boldsymbol{w}\cdot\nabla)\boldsymbol{u}$, $(\boldsymbol{w}\cdot\nabla)\boldsymbol{w}$ after contraction with $\hat{\boldsymbol{w}}_{\boldsymbol{k}}$ as in (1.20). This contraction converts these quadratic nonlinearities into cubic nonlinearities.

To reduce the multiple cubic terms into a single cubic nonlinearity requires either raising or lowering the order of the component terms, a process that through the c_s and d_s (A14) effectively introduces a length scale of 2π into the nonlinear inequality analysis. If the s-order can be retained, then c_s is used and only $s>3/2$ analysis is required. We start with how this two s-order inner products are absorbed between a test function $\boldsymbol{w}$ and $B_{NL}(\cdot,\cdot)$,

$$|(B_{NL}(w,u),w)_{\dot{s}}| \leqslant c_s\|u\|_{\dot{s}+1}\|w\|_{\dot{s}}^2. \tag{A16}$$

However, to handle the nonlinear time inequality needed to find the ν_s in $H_{\dot{s}}$, d_s and $s\geqslant 5/2$ are required. A rigorous argument from Constantin & Foias (1988) shows how order reduction of the inequality analysis can be done when higher-order $s>5/2$ is used. Specifically, the order $s+1$ terms can be reduced to order s by using the constant d_s (A14), so that the $\|\cdot\|_{\dot{s}+1}$ terms in (A16) are converted into following $\|\cdot\|_{\dot{s}}$,

$$|(B_{NL}(w,w),w)_{H^{\dot{s}}}| \leqslant d_s\|w\|_{\dot{s}}^3 \quad\text{and}\quad |(B_{NL}(u,w),w)_{H^{\dot{s}}}| \leqslant d_s\|u\|_{\dot{s}}\|w\|_{\dot{s}}^2. \tag{A17}$$

The first term converts the $B_{NL}(w,w)$ term into $\|w\|_{\dot{s}}^3$, a cubic nonlinearity, and the second allows the $B_{NL}(u,w)$ term to be paired with the $B_{NL}(w,u)$ term to form an integrating factor.

The next steps reduce the two viscous terms into a single term on the right-hand side using Young's inequality $ab\leqslant(1/2)(\epsilon a^2+(b^2/\epsilon))$ with $\epsilon=1/2$ to combine the first term on the right with the $\nu\|w\|_{s+1}^2$ on the left. Then, the last two terms are combined by using Cauchy–Schwarz upon the left one, that is, $d_s\|u\|_{\dot{s}}\leqslant Lc_s\|u\|_{\dot{s}+1}$ to get

$$\frac{1}{2}\underbrace{\frac{\mathrm{d}}{\mathrm{d}t}\|w\|_{\dot{s}}^2}_{L^{5-2s}T^{-3}} \leqslant \underbrace{\frac{\nu}{4}\|u\|_{\dot{s}+1}^2}_{(L^2T^{-1})(L^{3-2s}T^{-2})} + \underbrace{d_s\|w\|_{\dot{s}}^3}_{(L^{-5/2+s})(L^{15/2}T^{-3})L^{-3s}} + \underbrace{2c_s}_{M_s\sim L^{-3/2+s}}\underbrace{\|u\|_{\dot{s}+1}\|w\|_{\dot{s}}^2}_{(L^{15/2}T^{-3})L^{-3s-1}}. \tag{A18}$$

Underbraces are included to demonstrate the consistent order of each of its terms after the conversion of the $\|\cdot\|_{\dot{s}+1}$ (A16) into $\|\cdot\|_{\dot{s}}$ in (A17). (From a non-rigorous perspective, this effectively adds an inverse length that comes from the dependence of C_s (A14) upon L^{-1}.)

A.4. *Solving the difference inequalities for w with Euler u*

The last term on the right in (A18) can be used to create these integrating factors:

$$E_s(t)=\exp\left(\int_0^t M_s\|u(\tau)\|_{\dot{s}+1}\,\mathrm{d}\tau\right), \quad M_s=d_sL+c_s=s2^sC_{s-1}L+2^sC_s\,, \tag{A19}$$

https://doi.org/10.1017/jfm.2025.10513 Published online by Cambridge University Press

which with $C_s = L^{-3/2+s}$ becomes $M_s \sim s2^s L^{-3/2+s}$. This allows (A18) to be rewritten as

$$\frac{\mathrm{d}}{\mathrm{d}t}\left(E_s^{-2}(t)\|w(t)\|_{\dot{s}}^2\right) \leqslant \frac{\nu}{2}\|u\|_{\dot{s}+1}^2 E_s^{-2}(t) + 2d_s E_s(t)\|w\|_{\dot{s}}^3 E_s^{-3}(t). \tag{A20}$$

Then, by defining

$$X(t) = E_s^{-2}(t)\|w(t)\|_{\dot{s}}^2, \quad \alpha(t) = 2d_s E_s(t) \quad \text{and} \quad f(t) = \|u\|_{\dot{s}+1}^2 E_s^{-2}(t)\,, \tag{A21}$$

and using the following lemma, including the restrictions of (A23), (A25), (A26), one obtains an improved bound using $X(t)$.

LEMMA 1. *Suppose that $X \geqslant 0$ is continuous and*

$$\dot{X} \leqslant \alpha(t)X^{3/2} + (\nu/2)f(t), \quad X(0) = 0, \tag{A22}$$

for some $\alpha(\cdot) > 0$ and f positive and integrable on $[0, T]$. Then, for $X(t) < \infty$, assume

$$\nu\left(\int_0^t \alpha(s)\,\mathrm{d}s\right)\left(\int_0^t f(s)\,\mathrm{d}s\right)^{1/2} < 1; \tag{A23}$$

and by applying rules for integration by parts to the right-hand-side of (A22), one gets

$$X(t) \leqslant \frac{(\nu/2)\int_0^t f(\tau)\,\mathrm{d}\tau}{\left[1 - (2\nu)^{1/2}\left(\int_0^t \alpha(\tau)\,\mathrm{d}\tau\right)\left(\int_0^t f(\tau)\,\mathrm{d}\tau\right)^{1/2}\right]^2}, \tag{A24}$$

while

$$8\nu\left(\int_0^t \alpha(s)\,\mathrm{d}s\right)^2\left(\int_0^t f(s)\,\mathrm{d}s\right) \leqslant 1; \tag{A25}$$

and the following bound holds:

$$X \leqslant 2\nu\int_0^t f(s)\,\mathrm{d}s. \tag{A26}$$

Proof. Start with this overestimate. On the time interval $[0, T]$, the solutions $X(t)$ of (A22) are bounded above by the solution of

$$\dot{Y} = \alpha(t)Y^{3/2}, \quad Y(0) = (\nu/2)\int_0^T f(s)\,\mathrm{d}s. \tag{A27}$$

Now, simply observe that the solution $Y(t)$ of (A27) satisfies

$$\frac{1}{Y(0)^{1/2}} - \frac{1}{Y(t)^{1/2}} = 2\int_0^t \alpha(s)\,\mathrm{d}s, \tag{A28}$$

and hence,

$$Y(t) \leqslant \frac{Y(0)}{\left[1 - \int_0^t \alpha(s)\,\mathrm{d}s\,\left(2Y(0)^{1/2}\right)\right]^2}. \tag{A29}$$

Finally, by defining $Y(0)$ using (A27), one gets (A24). □

A.5. *Using the difference inequality solutions*

By re-inserting the definitions for $\alpha(t)$ and $f(t)$ (A21) into their time integrals (A25), one arrives at these conditions for critical viscosities ν_s (this determination of the ν_s, and the

https://doi.org/10.1017/jfm.2025.10513 Published online by Cambridge University Press

discussion in Appendices A.5 and A.6, follow earlier discussions with J. C. Robinson):

$$8\nu_s \underbrace{\left(\int_0^t 2d_s E_s(\tau)\,\mathrm{d}\tau\right)^2}_{(\int_0^t \alpha(\tau)\,\mathrm{d}\tau)^2} \underbrace{\int_0^t \|u(\tau)\|_{\dot{s}+1}^2 E_s^{-2}(\tau)\,\mathrm{d}\tau}_{\int_0^t f(\tau)\,\mathrm{d}\tau} = 1\,, \tag{A30}$$

such that all $\nu \leqslant \nu_s$ Navier–Stokes solutions are bounded by the Euler (u) solution when

$$\nu \leqslant \nu_s(t) = \frac{1}{8} \frac{1}{\underbrace{\left(\int_0^t 2d_s E_s(\tau)\,\mathrm{d}\tau\right)^2}_{L^{-5+2s}T^2} \underbrace{\int_0^t \|u(\tau)\|_{\dot{s}+1}^2 E_s^{-2}(\tau)\,\mathrm{d}\tau}_{L^{3-2s}T^{-1}}}\,, \tag{A31}$$

with the dimensions in the underbraces. When multiplied, these terms have the dimension of an inverse viscosity. Note that for any ν, at very early times when $\|w(t)\|_{\dot{s}} = \|v-u\|_{\dot{s}}$ and the $X(t)$ are small, these relations are irrelevant.

When critical viscosities ν_s equivalent to (A31) were first derived (Constantin 1986), the goal was to demonstrate the existence of this bound. Given our current understanding of the underlying Euler norms, can (A31) be used to estimate the ν_s in terms of time integrals of $\alpha(t)$ and $f(t)$?

A first step is to replace the time integrals with approximations at the ends of their respective time spans, with the $f(\tau)$ integral using $E_s^{-2}(\tau)$ focusing upon small times and the $\alpha(\tau)$ integral with $E_s(\tau)$ focusing upon on large times with $\mathrm{d}\tau \sim t$. By using these two limits to determine approximations, one can ignore intermediate times.

(i) For the integral with E_s^{-2}, note that $E_s^{-2}(t=0)=1$, so the approximation for E_s^{-1} depends on the $t \sim 0$ times $\delta\tau$ over which this is true. Giving for

$$E_s^{-2}(t) = \exp\left(-2\int_0^t M_s \|u(\tau)\|_{\dot{s}+1}\,\mathrm{d}\tau\right) \sim \mathcal{O}(1), \tag{A32}$$

$\Delta\tau \sim (2M_s\|u_0\|_{\dot{s}+1})^{-1}$ as $E_s^{-2}(t)$ becomes exponentially small. Then, with $f(t)$ from (A21),

$$\int_0^t f(\tau)\,\mathrm{d}\tau \approx \int_0^t \|u(\tau)\|_{\dot{s}+1}^2 E_s^{-2}(\tau)\,\mathrm{d}\tau \sim \|u(0)\|_{\dot{s}+1}^2/(2M_s\|u_0\|_{\dot{s}+1}) = \|u(0)\|_{\dot{s}+1}/(2M_s). \tag{A33}$$

(ii) For large t in $\alpha(t)$ (A21) and assuming that for the time span in question the $|u(\tau)\|_{\dot{s}+1}$ is very large, so the largest $\tau \sim t$ contributions to

$$E_s(t) = \exp\left(\int_0^t M_s\|u(\tau)\|_{\dot{s}+1}\,\mathrm{d}\tau\right) \quad \text{come over the last} \quad \Delta\tau \sim (M_s\|u(t)\|_{\dot{s}+1})^{-1}. \tag{A34}$$

(iii) This results in

$$\int_0^t \alpha(\tau)\,\mathrm{d}\tau = \int_0^t 2d_s E_s(\tau)\,\mathrm{d}\tau \sim 2d_s E_s(t)/(M_s\|u(t)\|_{\dot{s}+1}). \tag{A35}$$

Putting (A33) and (A35) together in (A31), that is, determining $(8(\int_0^t \alpha(t)\,\mathrm{d}t)^2 (\int_0^t f(t)\,\mathrm{d}t)^{-1}$, the resulting $(2\pi)^3$ domain, s-order $\nu_{s_{2\pi}}$ bounds for ν are given by

https://doi.org/10.1017/jfm.2025.10513 Published online by Cambridge University Press

$$\nu \leqslant \nu_{s_{2\pi}}(t) \sim \left[8 \left(2d_s E_s(t) \left(M_s \|u(t)\|_{\dot{s}+1} \right)^{-1} \right)^2 \left(\|u(0)\|_{\dot{s}+1} \right) (2M_s))^{-1} \right]^{-1}. \quad \text{(A36)}$$

Combining the terms gives this estimate,

$$\nu_{s_{2\pi}}(t) \lesssim \frac{M_s^3 \|u(t)\|_{\dot{s}+1}^2}{16 d_s^2 \|u(0)\|_{\dot{s}+1}}. \quad \text{(A37)}$$

Finally, for $\nu \leqslant \nu_{s_{2\pi}}$, the $\|w(t)\|_{\dot{s}}^2$ differences between the Navier–Stokes and Euler solutions are governed by

$$\|w(t)\|_{\dot{s}}^2 \leqslant 2\nu \int_0^t \|u(r)\|_{\dot{s}+1}^2 \exp\left\{ 2 \int_r^t M_s \|u(\tau)\|_{\dot{s}+1} \, \mathrm{d}\tau \right\} \mathrm{d}r. \quad \text{(A38)}$$

This means that the $\nu \leqslant \nu_{s_{2\pi}}$ Navier–Stokes solutions are bounded by these integrals of the Euler solutions. So unless those Euler solutions have finite-time singularities, and Meng & Yang (2024) suggests they do not, those Euler integrals will always be bounded, which in turn bounds the $\nu \leqslant \nu_{s_{2\pi}}$ Navier–Stokes solutions and in particular the dissipation rate $\nu Z(t) \to 0$.

Therefore, showing that Navier–Stokes solutions in $(2\pi)^3$ domains cannot develop finite energy dissipation in a finite time (1.2) as $\nu \to 0$.

Appendix A.6 extends this result to arbitrarity large $(2\ell\pi)^3$ domains, with the $\nu_s \to 0$ as ℓ grows, which would allow a dissipation anomaly (1.2).

A.6. *Release squeezing*

To estimate the ν_s critical viscosities for a compact initial condition in larger domains $(2\ell\pi)^3$, the first step is to squeeze that compact state by $\lambda = \ell$ into a $(2\pi)^3$ domain. This also means rescaling the velocities and derivatives as in (A1) and the higher-s norms as in (A4) giving:

(i) $\|u_\lambda(\tau)\|_{s+1} = \lambda^s \|u_\ell(\tau)\|_{s+1}$ (A3) for both $\tau = 0$ and $\tau = t$;
(ii) next, create $(2\pi)^3$ integrating factors $E_{s,\lambda}(t)$ by putting the $\|u_\lambda(t)\|_{s+1}$ in E_s (A19);
(iii) note that because this operation is in a $L_0^3 = (2\pi)^3$ domain, the M_s terms in $E_{s,\lambda}(t)$ do not need to be rescaled;
(iv) then apply $\|u_\lambda\|_{s+1}$ and $E_{s,\lambda}$ to (A36) to get $\nu_{s_{2\pi}}$;
(v) use the inverse of $\nu_\lambda = \nu/\lambda^2$ (A1), with $\nu_\lambda = \nu_{s_{2\pi}}$ and $\nu = \nu_s$: giving $\nu_s = \lambda^2 \nu_{s_{2\pi}}$;
(vi) this leads to the following ν_s in the original domain:

$$\nu_s(t) \sim \exp\left(- \int_0^t \lambda^{s+1} \|u_\ell(\tau)\|_{\dot{s}+1} \, \mathrm{d}\tau \right) \lambda^3 \frac{M_s^3 \|u_\ell(t)\|_{\dot{s}+1}^2}{16 d_s^2 \|u_\ell(0)\|_{\dot{s}+1}} \quad \text{(A39)}$$

with the exponentially decreasing factor dominating over the algebraic λ^3 term. This decrease of the ν_s as ℓ increases is more than fast enough to support the relevance of the variable domain calculations in figure 2.

References

Brachet, M.E., Meiron, D.I., Orszag, S.A., Nickel, B.G., Morf, R.H. & Frisch, U. 1983 Small-scale structure of the Taylor–Green vortex. *J. Fluid Mech.* **130**, 411–452.

Constantin, P. 1986 Note on loss of regularity for solutions of the 3—D incompressible Euler and related equations. *Commun. Math. Phys.* **104**, 311–326.

Constantin, P. & Foias, C. 1988 *Navier–Stokes equations*. University of Chicago Press.

https://doi.org/10.1017/jfm.2025.10513 Published online by Cambridge University Press

DOERING, C.R. 2009 The 3D Navier-Stokes Problem. *Annu. Rev. Fluid Mech.* **41**, 109–128.
DONZIS, D., GIBBON, J.D., GUPTA, A., KERR, R.M., PANDIT, R. & VINCENZI., D. 2013 Vorticity moments in four numerical simulations of the 3D Navier–Stokes equations. *J. Fluid Mech.* **732**, 316331.
DUBRULLE, B. 2019 Beyond Kolmogorov cascades. *J. Fluid Mech.* **867**, P1–63.
ESCAURIAZA, L., SEREGIN, G. & SVERÁK, V. 2003 L3, ∞-solutions to the Navier–Stokes equations and backward uniqueness. *Russian Math. Surv.* **58**, 211–250.
EYINK, G.L. 2003 Local 4/5-law and energy dissipation anomaly in turbulence. *Nonlinearity* **17**, 137–145.
EYINK, G. & JAFARI, A. 2022 High Schmidt-number turbulent advection and giant concentration fluctuations. *Phys. Rev. Res.* **4**, 023246.
GALLAY, T. & SMETS, D. 2020 Spectral stability of inviscid columnar vortices. *Anal. Part. Diff. Equ.* **13**, 17771832.
HOWARD, L.N. & GUPTA, A.S. 1961 On the hydrodynamic and hydromagnetic stability of swirling flows. *J. Fluid Mech.* **14**, 463–476.
ISHIHARA, T., GOTOH, T. & KANEDA, Y. 2009 Study of high–Reynolds number isotropic turbulence by direct numerical simulation. *Annu. Rev. Fluid Mech.* **41**, 165–180.
IYER, K.P., SREENIVASAN, K.R. & YEUNG, P.K. 2022 Nonlinear amplification of hydrodynamic turbulence. *J. Fluid Mech.* **930**, R2.
KERR, R.M. 1985 Higher-order derivative correlations and the alignment of small-scale structures in isotropic numerical turbulence. *J. Fluid Mech.* **153**, 31.
KERR, R.M. 1990 Velocity, scalar and transfer spectra in numerical turbulence. *J. Fluid Mech.* **211**, 309.
KERR, R.M. 2013*a* Swirling, turbulent vortex rings formed from a chain reaction of reconnection events. *Phys. Fluids* **25**, 065101.
KERR, R.M. 2013*b* Bounds for Euler from vorticity moments and line divergence. *J. Fluid Mech.* **729**, R2.
KERR, R.M. 2018*a* Trefoil knot timescales for reconnection and helicity. *Fluid Dyn. Res.* **50**, 011422.
KERR, R.M. 2018*b* Enstrophy and circulation scaling for Navier–Stokes reconnection. *J. Fluid Mech.* **839**, R2.
KERR, R.M. 2018*c* Topology of interacting coiled vortex rings. *J. Fluid Mech.* **854**, R2.
KERR, R.M. 2023 Sensitivity of trefoil vortex knot reconnection to the initial vorticity profile. *Phys. Rev. Fluids* **8**, 074701.
KERR, R.M., MENEGUZZI, M. & GOTOH, T. 2001 An inertial range crossover in structure functions. *Phys. Fluids* **13**, 1985–1994.
KIDA, S. & TAKAOKA, M. 1994 Vortex reconnection. *Annu. Rev. Fluid Mech.* **26**, 169–189.
LERAY, J. 1934 Sur le mouvement d'un liquide visqueux emplissant l'espace. *Acta Mathematica* **63**, 193–248.
LUNDGREN, T.S. 1982 Strained spiral vortex model for turbulent fine structure. *Phys. Fluids* **25**, 2193.
MENG, Z. & YANG, Y. 2024 Lagrangian dynamics and regularity of the spin Euler equation. *J. Fluid Mech.* **985**, A34.
NECAS, J., RUZICKA, M. & SVERÁK, V. 1996 On Leray's self-similar solutions of the Navier–Stokes equations. *Acta Mathematica* **176**, 283–294.
ONSAGER, L. 1949 Statistical hydrodynamics. *Il Nuovo Cimento* **6**, 279.
OSTILLO-MONICO, R., MCKEOWN, R., BRENNER, M.P., RUBINSTEIN, S.M. & PUMIR, A. 2021 Cascades and reconnection in interacting vortex filaments. *Phys. Rev. Fluids* **6**, 074701.
ROBINSON, J.C., RODRIGO, J.L. & SADOWSKI, W. 2016 *The Three-Dimensional Navier–Stokes Equations*. Cambridge University Press.
ROBINSON, J.C. 2020 The Navier–Stokes regularity problem. *Phil. Trans. R. Soc. Lond. A* **378**, 20190526.
ROBINSON, J.C. 2021 Using periodic boundary condition to approximate the Navier–Stokes equations in R^3 and the transfer of regularity. *Nonlinearity* **34**, 7683.
SCHMITT, F., FUCHS, A., PEINKE, J. & OBLIGADO, M. 2024 A universal relation between intermittency and dissipation in turbulence, arXiv: 2407.15953v1.
SREENIVASAN, K.R. 1984 On the scaling of the energy dissipation rate. *Phys. Fluids* **27**, 1048.
VASSILICOS, J.C. 2015 Dissipation in turbulent flows. *Annu. Rev. Fluid Mech.* **47**, 95–114.
YAO, J. & HUSSAIN, F. 2020 A physical model of turbulence cascade via vortex reconnection sequence and avalanche. *J. Fluid Mech.* **883**, A51.
YAO, J. & HUSSAIN, F. 2022 Vortex reconnection and turbulence cascade. *Annu. Rev. Fluid Mech.* **54**, 317–347.
YAO, J., YANG, Y., HUSSAIN, F. 2021 Dynamics of a trefoil knotted vortex. *J. Fluid Mech.* **923**, A19.
ZUCCOLI, E., BRAMBLEY, E. & BARKLEY, D. 2024 Trapped free surface waves for a Lamb–Oseen vortex flow. *J. Fluid Mech.* **997**, A40.

https://doi.org/10.1017/jfm.2025.10513 Published online by Cambridge University Press